Monthly Notices
of the
ROYAL ASTRONOMICAL SOCIETY

MNRAS **531,** 4464–4481 (2024)
Advance Access publication 2024 June 24

https://doi.org/10.1093/mnras/stae1367

Trio of super-Earth candidates orbiting K-dwarf HD 48948: a new habitable zone candidate

S. Dalal,[1★] F. Rescigno,[1] M. Cretignier,[2] A. Anna John,[3] F. Z. Majidi,[4,5,6] L. Malavolta,[4,5] A. Mortier,[7] M. Pinamonti,[5] L. A. Buchhave,[8] R. D. Haywood,[1†] A. Sozzetti,[5] X. Dumusque,[9] F. Lienhard,[10] K. Rice,[11,12] A. Vanderburg,[13] B. Lakeland,[1] A. S. Bonomo,[5] A. Collier Cameron,[4,14] M. Damasso,[5] L. Affer,[15] W. Boschin,[16,17,18] B. Cooke,[19,20] R. Cosentino,[18] L. Di Fabrizio,[16] A. Ghedina,[16] A. Harutyunyan,[16] D. W. Latham,[21] M. López-Morales,[21] C. Lovis,[9] A. F. Martínez Fiorenzano,[16] M. Mayor,[9] B. Nicholson,[22] F. Pepe,[9] M. Stalport,[23,24] S. Udry,[9] C. A. Watson[25] and T. G. Wilson[4,14]

Affiliations are listed at the end of the paper

Accepted 2024 May 23. Received 2024 May 22; in original form 2024 February 9

ABSTRACT

We present the discovery of three super-Earth candidates orbiting HD 48948, a bright K-dwarf star with an apparent magnitude of $m_V = 8.58$ mag. As part of the HARPS-N Rocky Planet Search programme, we collect 189 high-precision radial velocity measurements using the HARPS-N spectrograph from 2013 October 6, to 2023 April 16. Various methodologies are applied to extract the radial velocities from the spectra, and we conduct a comprehensive comparative analysis of the outcomes obtained through these diverse extraction techniques. To ensure the robustness of our findings, we employ several methods to address stellar variability, with a focus on Gaussian Process regression. To account for the impact of stellar variability and correlated noise in the radial velocity data set, we include activity indicators, such as $\log R'_{\rm HK}$ and bisector span, in the multidimensional Gaussian Process regression. Our analysis reveals three planetary candidates with orbital periods of 7.3, 38, and 151 d, and minimum masses estimated at 4.88 ± 0.21 M$_\oplus$, 7.27 ± 0.70 M$_\oplus$, and 10.59 ± 1.00 M$_\oplus$, respectively. The outermost planet resides within the (temperate) habitable zone, positioned at a projected distance of 0.029 arcsec from its star. Given the close proximity of this planetary system, situated at a distance of 16.8 parsecs, HD 48498 emerges as a promising target (closest super-Earth around FGK stars) for future high-contrast direct imaging and high-resolution spectroscopic studies.

Key words: techniques: radial velocities – planets and satellites: detection – stars: activity – methods: statistical – stars: rotation – instrumentation: spectrographs.

1 INTRODUCTION

In the past decades, a remarkable diversity of planetary systems has been revealed, revolutionizing our understanding of exoplanetary systems. A particular surprise was the discovery that super-Earths and sub-Neptunes are the most common type of planet, despite not being present in the Solar system. Super-Earths are characterized by radii ranging $1\,\mathrm{R}_\oplus \lesssim R_p \lesssim 2\,\mathrm{R}_\oplus$ (Fulton et al. 2017; Van Eylen et al. 2018) and masses within the range of $2\,\mathrm{M}_\oplus \lesssim M_p \lesssim 10\,\mathrm{M}_\oplus$ (Stevens & Gaudi 2013). On the other hand, sub-Neptunes have radii in the range of $2\,\mathrm{R}_\oplus \lesssim R_p \lesssim 4\,\mathrm{R}_\oplus$ with masses generally greater than 10 M$_\oplus$.

Building on the success of the High Accuracy Radial Velocity Planet Searcher (HARPS), its Northern hemisphere equivalent counterpart, High Accuracy Radial Velocity Planet Searcher – North (HARPS-N), was developed (Cosentino et al. 2012, 2014). Initially, the primary objective of the Guaranteed Time Observation (GTO) granted to the HARPS-N consortium was to follow up and characterize *Kepler*/K2 candidates (Borucki et al. 2010; Howell et al. 2014), but was later expanded to include candidates from the Transiting Exoplanet Survey Satellite mission (Ricker et al. 2015) and synergies with the CHaracterizing ExOPlanets Satellite mission (Benz et al. 2021). This programme enabled the determination of planetary bulk densities, which are crucial for atmospheric studies and for understanding the formation and evolution of planets (e.g. Rajpaul, Buchhave & Aigrain 2017; Malavolta et al. 2018; Bonomo et al. 2019; Cloutier et al. 2020; Mortier et al. 2020; Lacedelli et al. 2021).

The HARPS-N GTO programme also includes a Rocky Planet Search (RPS) that has the goal of searching for low-mass planets orbiting bright and nearby stars, with low levels of magnetic activity. To achieve this goal, each star is observed every night with a 15-min exposure time in order to minimize the impact of p modes and, if time allows, twice per night to mitigate the effect of granulation (Dumusque et al. 2011; Chaplin et al. 2019). The first results of the RPS programme were presented in Motalebi et al. (2015), who detected four low-mass planets around a nearby (6.5 pc) bright

---

[★] E-mail: s.dalal@exeter.ac.uk

[†] STFC Ernest Rutherford Fellow.

star HD 219134. Further details about the RPS programme, its sample, and its observational strategy can also be found in Motalebi et al. (2015). The re-evaluation of the RPS sample, prompted by recent enhancements in the Data Reduction Software (DRS) and the removal of specific HARPS-N systematics through the analysis of solar data (Dumusque et al. 2021), has revealed several potential new exoplanet candidates. For instance, HD 79 211b (10.6 $M_{\oplus}$) was found in the Habitable Zone in a 24.4-d orbit (DiTomasso et al. 2023); HD 99 492c, an additional planetary candidate was found after deeper reanalyses of the system (Stalport et al. 2023). Recently, Anna John et al. (2023) detected promising signals at sub m s^{-1} around the RPS target HD 144579.

One of the major challenges in detecting signals at sub m s^{-1} amplitudes is stellar variability, which can induce correlated radial-velocity (RV) signals with amplitudes of 0.1−100 m s^{-1} and time-scales that span seconds to decades (Crass et al. 2021). There have been several controversial detections where stellar activity was mistaken for planets, such as in the cases of α Cen B b (Dumusque et al. 2012; Hatzes 2013; Rajpaul, Aigrain & Roberts 2016), and GJ581 d and g (Vogt et al. 2010; Robertson & Mahadevan 2014). Therefore, it is crucial to carefully account for stellar variability when interpreting RV signals in blind searches for exoplanets. To mitigate the impact of stellar variability, diverse techniques have been developed, including spectral-level data reduction approaches like YARARA (Cretignier et al. 2021, 2023) and methods operating within the cross-correlation function (CCF) domain such as SCALPELS and TWEAKS (Collier Cameron et al. 2021; Anna John et al. 2023). Additionally, Gaussian Process (GP) regression has been used in RV surveys to model correlated stellar noise through the application of physically motivated kernels (Haywood et al. 2014; Rajpaul et al. 2015; Barros et al. 2020).

In this study, we present the detection of three planetary candidates orbiting HD 48948, a K-dwarf star. This new discovery reveals the presence of three super-Earth candidates. We observe HD 48 948 as part of the RPS programme using the HARPS-N spectrograph, as detailed in Section 2. Subsequently, we determine the stellar properties of the host star, as elaborated in Section 3. We extract radial velocities using two pipelines, as presented in Section 4. A comprehensive periodogram analysis, as detailed in Section 5, enables the detection of three significant signals. In Section 6, we analyse the activity indicators. To further model our data, we employ Keplerian models for these three dominant signals and apply two distinct GP analyses in Section 7. We also present an independent analysis of the system using TWEAKS in Section 8. We compare our results obtained from different analyses in Section 9. Finally, We summarize our results on the planetary candidates that we detect around HD 48 948 in Section 10. We provide a conclusion on our findings in Section 11.

2 OBSERVATIONS

As part of the RPS programme, the HARPS-N spectrograph was used to observe HD 48 948 from 2013 October 6 to 2023 April 16. HARPS-N is a high-precision echelle spectrograph on the 3.57 m Telescopio Nazionale Galileo on La Palma Island, Spain. It has stability and control features for pressure and temperature, which reduce instrumental drifts and allow the spectrograph to achieve sub-m s^{-1} precision in RV measurements over long periods of time (Cosentino et al. 2012, 2014). The instrument has a resolving power of 115 000 ($\frac{\Delta\lambda}{\lambda}$) and covers the wavelength range from 3800 to 6900 Å. We took 15-min exposures of HD 48 948 following the RPS programme's observational strategy. We obtained 189 spectra, each binned nightly, with a signal-to-noise (S/N) ratio per pixel at 527 nm typically falling within the range of 110–160, with an average of 140.

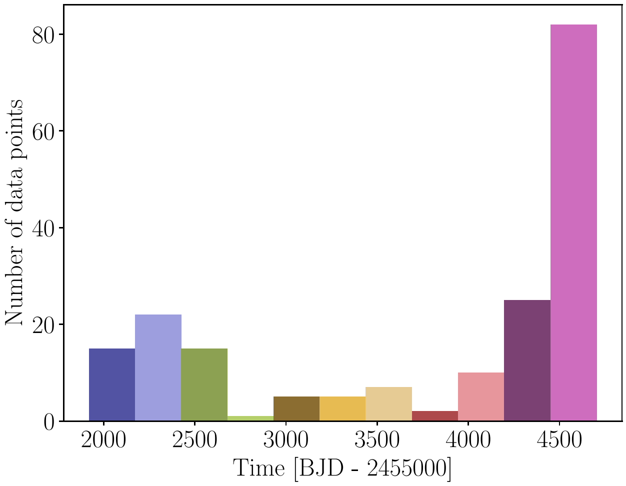

Figure 1. The histogram displays the number of observations per semester from 2013 October to 2023 April. Each bar shows the number of observations taken in each semester over the 10-yr period.

In Fig. 1, we present a histogram that illustrates the distribution of observations taken during each semester. From the histogram, one sees that 50 per cent of the observations were taken in the last two semesters. Prior to the last semester, the star was observed randomly, without any specific observation strategy, which led to poor coverage of phases of the possible signals in the radial velocity. During the initial analysis, hints of potential candidates were observed, and a dedicated observational strategy was then implemented to confirm these signals. To correct for the stellar variability using GP regression, we need to sample the stellar rotation cycle adequately. In the last semester, we aimed to detect these signals across all phases and sample the stellar rotation. The adoption of these new observational strategies has notably enhanced the significance of all potential planetary signals.

3 STELLAR CHARACTERISTICS

HD48948 is a K-dwarf star located at a distance of 52.18 light years (Gaia Collaboration 2023) from Earth. The star is moderately active, with a mean log R'_{HK} of −4.915 dex. It has a $B-V$ colour of 1.21 mag (van Leeuwen 2007). We also compute the $B-V$ value using the colour–temperature relation for stars (Sekiguchi & Fukugita 2000) and obtain a value of 1.04 mag. Using the activity–rotation relationship outlined in Mamajek & Hillenbrand (2008), we derive the stellar rotation period (P_{rot}) from log $R'_{\mathrm{HK}} = -4.915$ and $B-V = 1.04$ to be 46.1 ± 6.1 d. We used high-quality HARPS-N spectra to obtain stellar atmospheric parameters. Following the procedure outlined in detail in Mortier et al. (2020), we apply three separate methods: ARES + MOOG, SPC, and CCFPams. The final stellar parameters, as listed in Table 1, were derived through a weighted average of the results from the three methods, with weights assigned according to the inverse variance.

ARES + MOOG: The first method, ARES + MOOG, uses the co-added spectrum shifted in the lab-frame. It is a curve-of-growth method employing a line list of neutral and ionized iron lines (Sousa 2014). We used a specific line list for cool dwarf stars (Tsantaki et al. 2013) and the method implementation through FASMA (An-

Table 1. Stellar parameters for HD 48948.

Parameter		Value	Source
RA	[h m s]	06 49 57.57	*Gaia* DR3
Dec.	[d m s]	+60 20 14.53	*Gaia* DR3
Spectral type		K3V	Simbad
$B - V$		1.21	HIPPARCOS
J		6.33 ± 0.02	2MASS
H		5.73 ± 0.02	2MASS
K		5.61 ± 0.02	2MASS
$W1$		5.64 ± 0.13	AllWISE
$W2$		5.51 ± 0.06	AllWISE
$W3$		5.56 ± 0.02	AllWISE
Parallax	(mas)	59.393 ± 0.025	*Gaia* DR3
Distance	(pc)	16.837 ± 0.007	*Gaia* DR3
T_{eff}	(K)	4593 ± 60	This work
[Fe/H]	(dex)	-0.21 ± 0.03	This work
ξ_t	(km s^{-1})	0.14 ± 0.03	This work
$v \sin i$	(km s^{-1})	< 2	This work
$\log g_{\mathrm{spec}}$	(dex)	4.59 ± 0.08	This work
$\log g_{\mathrm{iso}}$	(dex)	4.61 ± 0.01	This work
Mass	[M$_\odot$]	$0.686^{+0.020}_{-0.013}$	This work
Radius	[$R_\odot$]	$0.679^{+0.004}_{-0.004}$	This work
ρ_* [$\rho_\odot$]		$2.18^{+0.069}_{-0.033}$	This work
Age	(Gyr)	$11.48^{+1.93}_{-4.67}$	This work
$\log R'_{\mathrm{HK}}$	(dex)	-4.915	This work
P_{rot}	(days)	$43.45^{+1.00}_{-0.71}$	Section 7

Note. Gaia DR3 – Gaia Collaboration (2023); Simbad – Grieves et al. (2018); HIPPARCOS – van Leeuwen (2007); 2MASS – Skrutskie et al. (2006); AllWISE – Wright et al. (2010), Cutri et al. (2013).

dreasen et al. 2017). We find that the stellar effective temperature is $T_{\mathrm{eff}} = 4584 \pm 83$ K, the surface gravity is $\log g = 4.60 \pm 0.22$ dex, the microturbulence is $\xi_t = 0.14 \pm 0.03$ km s^{-1}, and the metallicity [Fe/H] is -0.13 ± 0.04 dex. We did not correct the surface gravity for accuracy (Mortier et al. 2014) because the recommended correction is only well established for stars with higher effective temperatures.

SPC: Secondly, we use a spectrum synthesis method, the Stellar Parameter Classification tool (SPC: Buchhave et al. 2012). SPC is run on each individual spectrum, and shows very good consistency between individual results. The observed spectra are cross-correlated with a library model template spectra and the individual results are then combined using a weighted average using the normalized cross-correlation function as weights. Surface gravity was constrained using Yonsei–Yale (YY) isochrones. We find that $T_{\mathrm{eff}} = 4495 \pm 50$ K, $\log g = 4.65 \pm 0.10$ dex, and [Fe/H] $= -0.22 \pm 0.08$ dex. Unlike the previous approach, SPC allows us to derive a projected rotational velocity value, and we determine it to be $v \sin i < 2$ km s^{-1} ($P_{\mathrm{rot}} >$ 17 d), consistent with the stellar rotation period ($\sim$ 48 d).

CCFpams: Thirdly, we obtained atmospheric parameters by using the CCFs and an empirical calibration between the equivalent width of the CCF and the atmospheric parameters. This method is detailed in Malavolta et al. (2017). We find that $T_{\mathrm{eff}} = 4699 \pm 150$ K, $\log g = 4.53 \pm 0.06$ dex, and [Fe/H] $= -0.28 \pm 0.05$ dex.

The results of all three independent methods are fully compatible within errors. After having obtained the atmospheric parameters, we use the effective temperature and metallicity to obtain stellar mass, radius, and age. We note that we did not use the spectroscopically obtained surface gravity ($\log g_{\mathrm{spec}}$), as it can sometimes be inaccurate (e.g. Torres et al. 2012; Mortier et al. 2014). Additionally, we used the *Gaia* DR3 parallax and eight photometric apparent magnitudes obtained from various sources. Specifically, we used magnitudes from HIPPARCOS ($B - V$), 2MASS (J, H, K), and AllWISE ($W1$, $W2$, $W3$) data sets (Skrutskie et al. 2006; van Leeuwen 2007; Wright et al. 2010; Cutri et al. 2013).

The code `isochrones` (Morton 2015) was used to obtain posterior samples for stellar mass, radius, and age and thus also provides a new value for surface gravity ($\log g_{\mathrm{iso}}$). The code was run six times, using the individual spectroscopic results and employing two different stellar evolution models, namely Dartmouth and MESA Isochrones and Stellar Tracks (MIST; Dotter 2016) in order to take into account different model systematics (see e.g. Tayar et al. 2022). Subsequently, all the resulting samples were combined to obtain the final adopted parameters, extracted as the median of the combined posterior distribution. This procedure is also outlined in Mortier et al. (2020). All individual results agree well, and the final parameters are shown in Table 1.

4 RADIAL VELOCITY OBSERVATIONS

We used the 2.3.5 version of the HARPS-N DRS pipeline to reduce the data, employing the cross-correlation technique (Baranne et al. 1996; Pepe et al. 2002). The pipeline provides precise RVs and estimates parameters directly from the spectrum's CCF. These parameters include the CCF full width at half-maximum (FWHM), CCF contrast, CCF bisector span inverse slope (BIS). Additionally, the pipeline provides measurements of S-index, H α, Na, and $\log R'_{\mathrm{HK}}$ derived from the spectrum.

In our pursuit of detecting small planets that induce small RV shifts, stellar variability presents a challenge. We know that the activity of the host star can either obscure or imitate the RV signals caused by planets, leading to contentious detections (Vogt et al. 2010; Dumusque et al. 2012). The upper panel in Fig. 3 shows the Generalized Lomb–Scargle (GLS) periodogram of DRS RVs. The primary peak in the periodogram corresponds to the instrumental systematics occurring approximately every 1400 d, a pattern consistent with the RVs of RPS targets as observed in Anna John et al. (2023). Moreover, this star exhibits moderate activity, with a stellar rotation period of around 48 d, potentially obscuring the planetary signals. To tackle this issue, we have opted to employ specialized post-processing tools tailored to mitigate the influence of stellar activity in the radial velocity data. Specifically, we applied YARARA and TWEAKS (Time and Wavelength-domain stEllar Activity mitigation using Kima and Scalpels), following the methods outlined by Cretignier et al. (2021, 2023) and Anna John et al. (2023). However, for the scope of this research paper, we will primary focus on the RVs obtained through the YARARA technique. Further details of our analysis using the TWEAKS approach are provided in Section 8.

YARARA (Cretignier et al. 2021) is a post-processing method based on spectra time-series correction. The method aims to correct for various contaminations such as cosmic rays, telluric lines, stellar activity, and instrumental systematics (interference patterns, point spread function variations, fibre B contamination and ghosts). The code works with one-dimensional order-merged spectra produced by the official DRS that are continuum normalized with the publicly available code RASSINE (Cretignier et al. 2020b). A master spectrum $S_{\mathrm{ref}}(\lambda)$ is built by stacking the individual spectra and used to derive the residual spectra time-series $\delta S(\lambda, t) = S(\lambda, t) - S_{\mathrm{ref}}(\lambda)$. Most of the time and flux variations in that space are corrected by multilinear regressions in flux, either performed in the stellar, or terrestrial rest frame. For instance, the stellar activity is corrected by fitting a scaled version of the S-index on each wavelength column of the spectra time-series matrix since stellar lines vary in first-order like the S-

Table 2. This table lists the correction applied by each pipeline to produce different RV data sets.

RV data set	YV2	YVA	TWEAKS
Input	Spectrum	Spectrum	CCF
Use	Section 7.1	Sections 7.2 and 7.3	Section 8
Magnetic cycle	Yes	No	Yes
Rotation modulations	Yes*	No	Yes*
Instrumental systematic	Yes†	Yes†	Yes†
Reference	C21	C21	A23

*There might still be residual rotational modulation at the harmonics of stellar rotation periods.

†The data set may still exhibit long-term instrumental systematic effects. C21, Cretignier et al. (2021); A23, Anna John et al. (2023).

index (Basri, Wilcots & Stout 1989; Wise et al. 2018; Cretignier et al. 2021). The correction of the point spread function (PSF) was obtained as in Stalport et al. (2023) by extracting symmetric PSF variations of the CCFs decorrelated from the S-index. We call RVs obtained from YARARA corrected spectra the YARARA Version 1 (YV1) RVs. Note that any systematic correction applied by YARARA can be easily re-implemented at the spectrum level. The reinjection of activity signals is robust because we are essentially reintroducing initially present, filtered-out signals, considering YARARA is a multilinear framework. We use this approach to generate a data set that has been corrected for instrumental systematics, but with the activity re-injected. This data set is known as the YVA RVs.

Once spectra are flux corrected, line-by-line (LBL) RVs were extracted as described in Dumusque (2018). This was done using an optimized line selection that matches the master spectrum of HD 48948, in a similar way to that in Cretignier et al. (2020a). Note that the same line list was used to compute the CCFs, where the weights in the masks were defined by the RV Doppler content of the spectral line, as defined in Bouchy, Pepe & Queloz (2001). Deeper lines are therefore overweighted in comparison to shallow lines, optimizing the RV extraction and minimizing the photon noise (Lafarga et al. 2020; Bourrier et al. 2021).

Further RV corrections are obtained by decorrelating the LBL RVs in a multilinear model using the shell time-series coefficients introduced in Cretignier, Dumusque & Pepe (2022) as well as the Principal Component Analysis (PCA) components introduced in Cretignier et al. (2023). The shell method maps the residual spectra time-series, denoted as $\delta S(\lambda, t)$, into a compact space represented as $\delta S(\partial S_{\mathrm{ref}}/\partial v,\ S_{\mathrm{ref}},\ t)$. This space enables the measurement of distortions in the line profile (along with their associated time-coefficients) that are orthogonal to pure Doppler shifts. On the other hand, the PCA on LBL RVs use the property that global shifts of the spectrum cannot be present in the main components of a PCA and will be planetary-free since pure Doppler shifts are mean effects without variance. Both the shell and LBL PCA, therefore, provide time-domain vectors that can be used to form a basis to fit the RVs. The RVs that are derived after decorrelation with this basis are referred to as YV2 RVs. This is in contrast to the YV1 RVs, which are obtained through correction in the wavelength domain. The vector basis that transitions from YV1 to YV2 comprises six vectors: three related to shell components and three associated with instrumental-related systematics. The limited number of components can be attributed to the constrained signal-to-noise ratio (S/N $\sim$ 130) of HD 48 948 that prevents an optimal extraction of time-domain vectors by PCA.

Throughout the paper, we will primarily use the YV2 RVs for our analysis, except when employing GP regression to model the radial velocity signal. The Table 2 provides a summary of the corrections applied by each pipeline to generate various radial velocity data sets. Fig. 2 shows the time series of the three RV data sets. The RV data sets include YV2, processed from spectra and used in Section 7.1, accounting for the magnetic cycle, potentially removing rotation modulations, and exhibiting the low instrumental systematic effects (Cretignier et al. 2021). The YVA data set, derived from spectra and used in Sections 7.2 and 7.3, does not correct for the magnetic cycle or rotation modulations, but has minimal instrumental systematic impact (Cretignier et al. 2021). Finally, the TWEAKS data set, obtained from CCF and used in Section 8, addresses the magnetic cycle, may involve rotation modulations, and has a moderate level of instrumental systematic effects (Anna John et al. 2023).

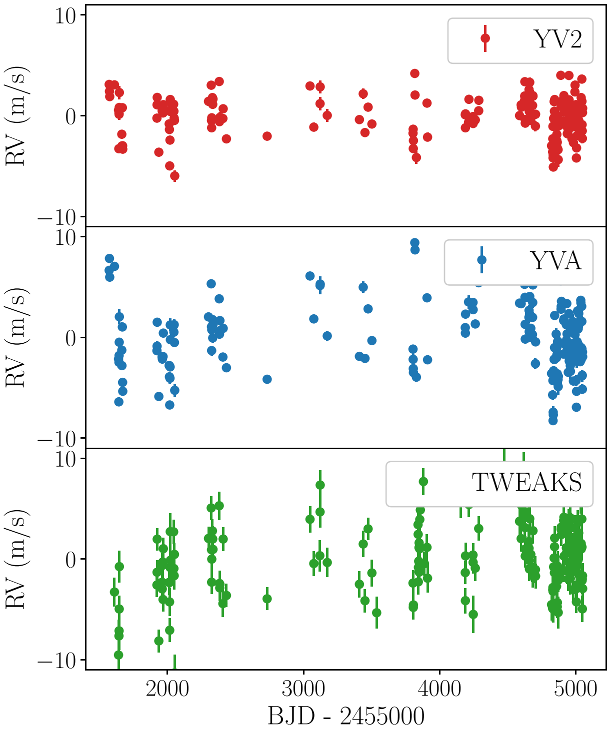

Figure 2. *RV time series:* The YV2 RVs are represented by solid red circles, the YVA RVs by solid blue circles, and the TWEAKS RVs by solid green circles, along with uncertainties on the RVs.

5 PERIODOGRAM ANALYSIS

We employ a variety of tools and software to investigate the primary signals present in YV2 RVs and stellar activity indicators, which include BIS, FWHM, S-index, H_{α}, and Na. We utilize both GLS (Zechmeister & Kürster 2009) and $\ell 1$ periodograms (Hara et al. 2017) to identify periodicities in the YV2 RV data. We also examine the Stacked Bayesian formalism for the generalized Lomb–Scargle periodogram (BGLS; Mortier & Collier Cameron 2017) to verify consistency of the signal. Furthermore, we analyse the window function to differentiate between the true frequency and aliases caused by other frequencies (see Section 7.2.1). A more detailed analysis is also conducted on the stellar activity indicators in Section 6.

GLS Periodogram: We calculate the GLS periodogram for the radial velocity data set to identify periodicities within irregularly sampled time series of HD 48948. In Fig. 3, we display the obtained GLS periodogram for HD 48 948 DRS RVs in solid black line and YARARA V2 RVs in solid red line. We detect significant signals with False Alarm Probability (FAP) < 0.01 per cent at periods of 7.3

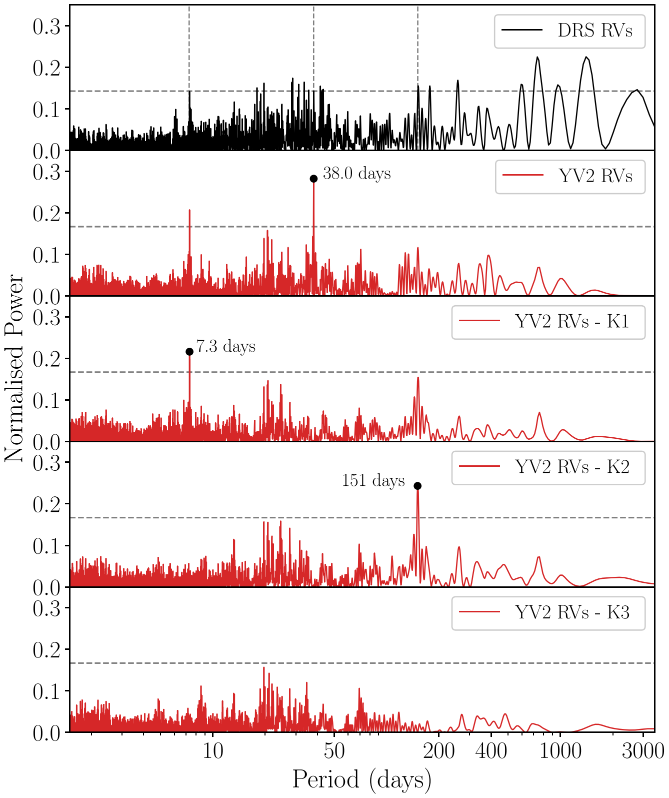

Figure 3. *GLS Periodograms of HD 48 948 DRS and* YARARA *V2 RVs*: The top panel displays the GLS periodogram of the DRS RVs, represented by a solid black line. All other panels show GLS periodogram of the YARARA V2 RVs. The first red line periodogram, calculated for all YARARA V2 RVs, shows the most significant peak at 38 d. The second red line periodogram, which represents the residual series after removing the dominant Keplerian signal at 38 d, reveals the highest peak at 7.3 d. The third red line periodogram, which shows the residuals after removing Keplerian signals at both 7.3 and 38 d, now has the highest peak at 151 d. The final panel shows the periodogram of the residuals after eliminating Keplerian signals at 7.3, 38, and 151 d. Each panel includes a horizontal dashed line representing an FAP of 0.01 per cent.

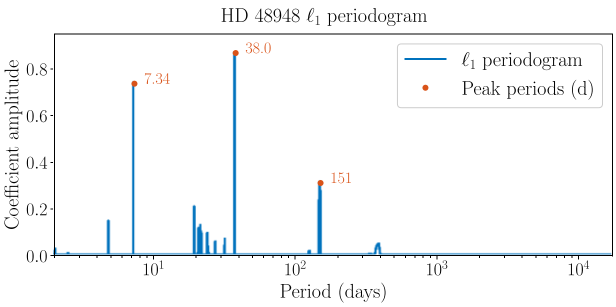

Figure 4. *ℓ1 Periodograms of HD 48 948* YARARA *V2 RVs:* The three planetary signals identified with highest $\log_{10}$ FAP at 7.3, 38, and 151 d are highlighted with a red dot.

and 38 d. After removing these two signals using two sinusoidal functions, we observe a prominent peak at a longer period of roughly 151 d. Finally, we find smaller peaks spanning a range of 20–22 d in the residual radial velocity, which could potentially be indicative of the star's half-rotation period.

ℓ1 Periodogram: We also compute the ℓ1 periodogram, which has a similar aspect as the Lomb–Scargle periodogram but has fewer peaks due to aliasing, as it simultaneously fits for all signals. Fig. 4 shows the ℓ1 periodogram for HD 48948. It is clear that the three dominant peaks in the radial velocity are at 7.3, 38, and 151 d. The $\log_{10}$ FAP for 7.3, 38, and 151 d are -4.62, -6.35, and -4.74, respectively.

Stacked BGLS Periodogram: We also present the stacked BGLS periodogram of radial velocity. Given that planetary signals tend to be stable and coherent, while stellar activity signals lack this consistency, we anticipate an enhancement in the strength of planetary signals as we add more data. Our observations confirm this trend for the three peaks we detect, as the peaks at 7.3, 38, and 151 d become more pronounced while incorporating additional radial velocity data, as shown in Fig. 5. In addition, the S-BGLS reveals the stellar rotation at 42.6 d and the strength of this signal does not consistently increase due to the quasi-periodic nature of activity cycles. This differs from planetary signals, which usually become stronger with more observations.

6 ACTIVITY INDICATORS

In this section, we analyse the activity indicators obtained from the co-added spectra. Our analysis begins with exploring the correlations among different activity indicators and radial velocity, followed by periodogram analysis of various activity indicators. Following this, we identify the magnetic cycle through the S-Index. Furthermore, we employ GP regression (see Section 7) to model one of the stellar activity proxies ($\log R'_{\mathrm{HK}}$), enhancing our understanding of the covariance structure underlying stellar-induced variability in RVs.

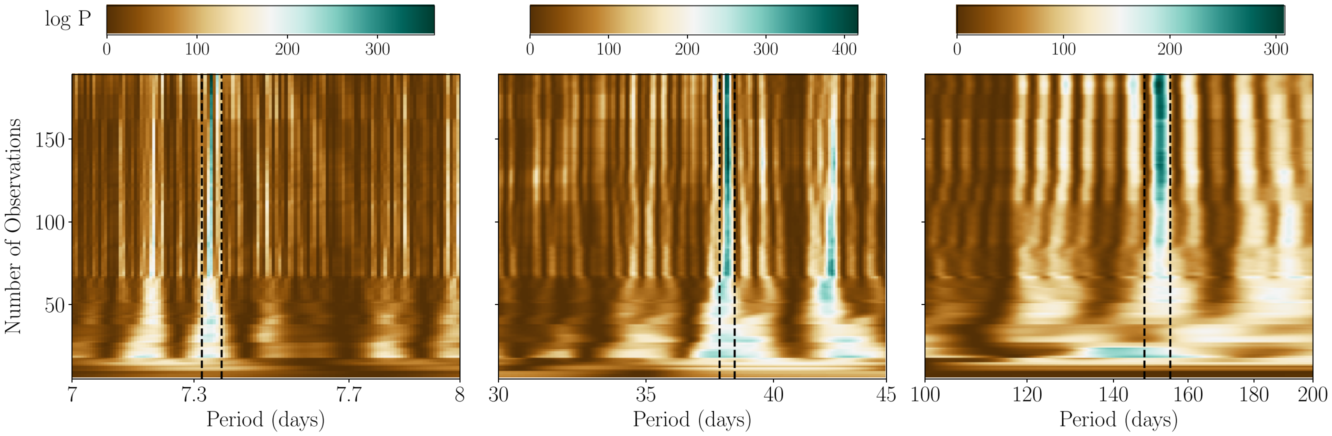

Figure 5. *S-BGLS periodograms of YV2*: The figure shows the S-BGLS periodograms of YV2 for the star HD48948 focusing on three frequency ranges (7.3, 38, and 151 d). The absolute value of log *P* is not meaningful; instead, the relative values of log P hold significance. The signal observed at approximately 42 d in the middle panel represents the unstable activity feature.

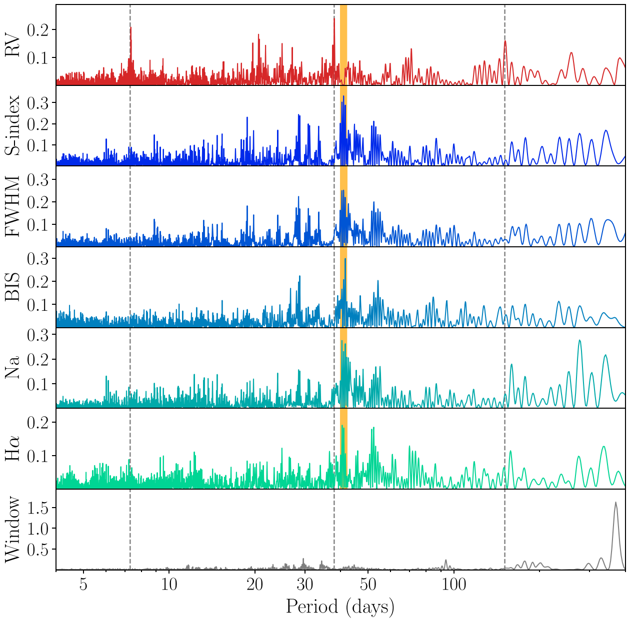

Figure 6. *GLS periodogram of activity indicators:* The figure presents the periodogram of various activity indicators, including the YARARA V2 RVs for the star HD 48948. Three significant peaks in the RV data are highlighted by dashed lines, corresponding to periods of 7.3, 38, and 151 d. The most significant peak in all activity indicators which is the stellar rotation period is represented by the region shaded in orange. The last panel shows the window function which highest peak around 365 d (1 yr alias).

Pearson correlation: We calculate the Pearson correlation coefficient to examine the relationship between the RV time series YVA and various activity indicators. The most significant correlation was observed with the S-index, yielding a coefficient of 0.55. This was closely followed by the FWHM, which had a correlation coefficient of 0.54. Other indicators such as bisector span, Na, and H_{α} demonstrated lower correlation coefficients of 0.33, 0.46, and 0.28, respectively.

Periodograms: Fig. 6 shows the periodogram of radial velocity YV2 and various activity indicators along with the window function. It is clear that the most significant peak in all the activity indicators is around 42–43 d, as highlighted by the orange shaded region. We find no peaks close to 7.3 and 151 d in the periodogram of any of the activity indicators. Given that the rotation period is very close to the period of one of the planetary candidates, we conduct a more detailed and robust analysis in Section 7.

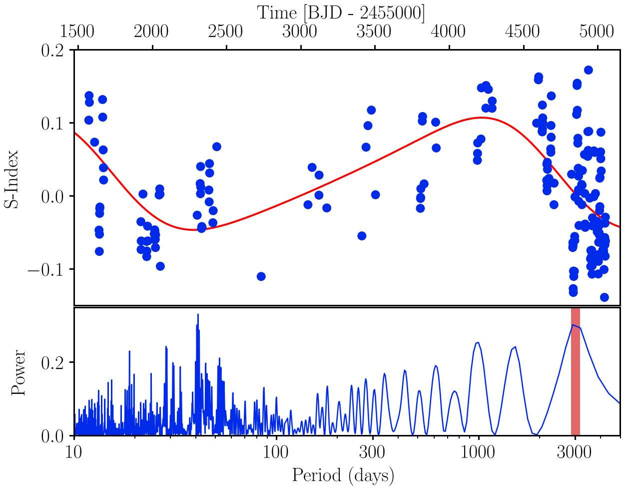

Figure 7. Top panel: The figure shows the S-index time series of HD 48 948 using blue solid circles, and the red line represents the best fit of the skew-sinosoidal model. Bottom panel: The Generalized Lomb–Scargle (GLS) periodogram for the S-index is plotted in blue line, with the red solid line aligning with the peak at approximately 3000 d (around 8.2 yr), corresponding to the period of the best-fitting model shown in the upper panel.

Magnetic cycle: Fig. 7 displays the S-Index time series for HD 48948, revealing a clear magnetic cycle. In the bottom panel of the figure, we present the GLS periodogram of the S-Index. Notably, one of the highest peaks, indicated by the red solid line, potentially corresponds to the period of the magnetic cycle, estimated to be around 3000 d. To determine the period of this magnetic cycle, we employed a skew-sinusoidal model.[1] The skew sinusoidal function

---

[1] A skew sin model (three parameters) compared to a Keplerian (five parameters) yield the same period (8.2 yr) for the magnetic cycle. We prefer to use a model with fewer parameters for simplicity and interpretability.

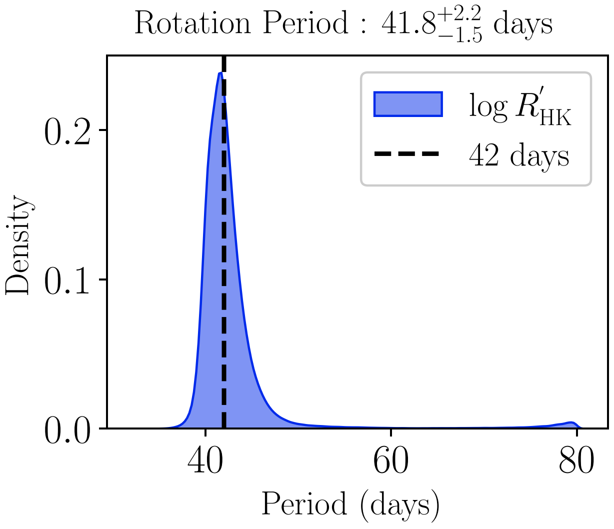

Figure 8. Posterior distribution of period of the quasi-periodic kernel after GP regression of the log $R'_{\rm HK}$ time series.

is expressed as

$$\mathrm{skew\,sin}\,(x, P, A, \phi) = A \sum_{n=1}^{4} a_n \sin\left(2\pi \frac{nx}{P} + \phi\right). \tag{1}$$

In this equation, A represents the amplitude, P denotes the period, and ϕ represents the phase. The coefficients a_n for the four sine terms are $\frac{7}{16}$, $\frac{7}{64}$, $\frac{1}{48}$, and $\frac{1}{512}$. Our analysis reveals an estimated magnetic cycle period of 8.2 yr for HD 48498.

Gaussian process: In order to further investigate the structure of the signals in the activity indicator, log $R'_{\rm HK}$ and to isolate the stellar rotational period, we applied a GP regression analysis. The signal in the activity indicator is modelled using a Quasi-Periodic kernel (details in Section 7.2). This analysis was done with MAGPY_RV[2] (Rescigno et al. 2023a; Rescigno, Dixon & Haywood 2023b), and the best-fitting kernel hyperparameters were identified via affine invariant MCMC optimization. We evolved 2000 chains over 1000 iterations, discarding a burn-in phase of 200 steps. All hyperparameters were constrained with a forced positive uniform prior. Additionally, we restricted the harmonic complexity to be between 0 and 1, the stellar rotation period to range from 0 to 60 d, and the jitter to vary between 0 and the highest uncertainty value within the given time series.

Fig. 8 shows the posterior distribution of the GP period. The result of our GP regression analysis indicates a stellar rotation period of $41.8^{+2.2}_{-1.5}$ d. The evolution timescale for log $R'_{\rm HK}$ was not well defined, resulting in values of 171^{+128}_{-66} d. The harmonic complexity was found to be 0.73 ± 0.19. In summary, the GP regression analysis of log $R'_{\rm HK}$ agrees with the results obtained from the periodogram analysis, confirming the presence of stellar rotation with a period of ~ 42 d. Furthermore, these findings can be used to further inform GP regression analyses of the RVs.

7 RV ANALYSIS

Given the intricate nature of the star's variability, we use multiple data sets and methodologies in our analysis to better understand our results. We start with YV2 RVs derived using PCA and use a simple model incorporating only the planetary signals, as detailed in Section 7.1. A PCA approach, which corrects for systematics (including stellar activity), is particularly beneficial when dealing with large data sets due to their lower computational demands. Furthermore, this method is less likely to absorb genuine planetary signals. However, it is important to note that PCA is sensitive to outliers, and there is a lack of understanding of which physical processes it corrects. We then analyse the YVA RVs and employ GP regression. We use the results from the activity indicator analysis to inform a one-dimensional GP regression analysis of the YVA RVs, as discussed in more detail in Section 7.2. GP models offer flexibility and robustness in modelling complex, poorly understood, or poorly constrained physical processes (Nicholson & Aigrain 2022). However, there are risks of overfitting, and thus the GP may partly or fully absorb the planetary signals (see Section 7.2.1). To limit this risk, we also conduct a multidimensional GP analysis which combines the information from both RVs and activity proxies, described in Section 7.3.

We examine three potential system configurations: one with three Keplerians, each having orbital periods of 7.3, 38, and 151 d, and two with two-Keplerian setups, where the Keplerians have orbital periods of 7.3 and 38 d, and 7.3 and 151 d, respectively. To fairly compare the final likelihoods of these three models, we employ the corrected Akaike Information Criterion,[3] known as AICc (Sugiura 1978; Akaike 1983). The AICc is calculated as follows:

$$\mathrm{AICc} = -2\ln\mathcal{L} + 2N_{\rm free} + 2\left(\frac{N_{\rm free}(1 + N_{\rm free})}{N_{\rm data} - N_{\rm free} - 1}\right). \tag{2}$$

Here, $\ln\mathcal{L}$ represents the maximized logarithmic likelihood obtained from the optimization process, $N_{\rm free}$ denotes the number of free parameters (e.g. 10 for the two-Keplerian model and 15 for the three-Keplerian model), and $N_{\rm data}$ signifies the total number of data points (i.e. 189). We also calculate the percentage likelihood, Φ, using

$$\Phi(\mathrm{AICc}, \mathrm{AICc}_{\rm ref}) = 100 \times \left[1 - \exp\left(-\frac{\mathrm{AICc} - \mathrm{AICc}_{\rm ref}}{2}\right)\right]. \tag{3}$$

This percentage quantifies the relative support for the model under consideration (AICc) compared to the reference model ($\mathrm{AICc}_{\rm ref}$), with higher values indicating stronger evidence in favour of the considered model. We assume that there is substantial evidence favoring one reference model over another when a 95 per cent confidence level is achieved, i.e. when $\mathrm{AICc} > \mathrm{AICc}_{\rm ref} + 6$ or $\Phi > 95$. The differences in AICc less than 4.5, which corresponds to less than 90 per cent confidence, are typically insufficient to reliably differentiate between two models based solely on statistical arguments (i.e. no astrophysics is involved; Vitral et al. 2022).

7.1 Keplerian only analysis

We begin our analysis by assuming that the YV2 data set is fully and successfully cleaned of all stellar activity signals, and it only maps the coherent motion due to gravitational interactions between the star and the planets in the system. Consequently, we model the RV data set by summing up Keplerian models, with each model representing an individual planet.

In our analysis, we use the code MAGPY_RV (Rescigno et al. 2023a; Rescigno et al. 2023b). The best-fitting model is determined through

---

[2] Available at https://github.com/frescigno/magpy_rv.

[3] As our model is an empirical fit rather than an exact representation of reality, we prioritize the AICc criterion, as recommended by Burnham & Anderson (2002), when comparing different models.

an iterative process using affine invariant Markov Chain Monte Carlo (MCMC) and logarithmic likelihood maximization. To expedite the process, we parallelize the code across multiple computing cores. For the MCMC iteration, we choose to re-parametrize eccentricities, e, and arguments of periastron, ω, in the form $\sqrt{e}\cos\omega$ and $\sqrt{e}\sin\omega$ (Eastman, Gaudi & Agol 2013). This re-parametrization avoids boundary conditions for circular orbits while maintaining uniform priors across the entire parameter space.

In terms of prior information, we apply uniform priors to each planetary orbital period based on the results of the periodogram analysis, with the width of each prior related to the width of the corresponding peak such that a wider peak has wider priors. Additionally, we impose a wide uniform prior equivalent to the orbital period on the time of periastron for the innermost planet to prevent multiple global minima results. All other parameters are bound by wide positive uniform priors.

For each of the three system configurations, we evolve 700 chains for 5000 iterations, with the first 1000 steps disregarded as burn-in. We also compute the likelihood and AICc values for each model, as presented in Table 5. It is evident from both the likelihood values and the AICc that the model with three Keplerians is strongly preferred by this data set. The results from this preferred model are detailed in Table 3, under the section 'Three Keplerians-only Analysis'. We find the orbital periods for the three Keplerians to be 7.34, 38.0, and 151 d with all having circular orbits. Their RV amplitudes are constrained to 7σ for Keplerian b, 8σ for Keplerian c and 6σ for Keplerian d. We also include their minimum mass in the Table 3.

7.2 One-dimensional GP analysis

We model the YVA RVs as a combination of multiple planetary signals, in the form of Keplerians, and stellar activity, in the form of a Quasi-Periodic kernel, as described in Haywood et al. (2014). The Quasi-Periodic kernel includes a white noise component and can be represented by the following equation:

$$k(t_i, t_j) = A^2 \cdot \exp\left[-\frac{|t_i - t_j|^2}{\tau^2} - \frac{\sin^2\left(\frac{\pi\cdot|t_i - t_j|}{P_{\mathrm{rot}}}\right)}{\mu^2}\right] + \delta_{i,j}\beta^2. \quad (4)$$

In this equation, $k(t_i, t_j)$ corresponds to the covariance function, A is the amplitude, τ denotes the timescale that governs the evolution of quasi-periodic variations and is closely associated with the changes occurring in active regions over time. P_{rot} is the period of the stellar rotation, while μ is a parameter that characterizes the harmonic complexity of the fit. Additionally, β serves as a jitter term, and its role is to model the contribution of white noise to the RVs derived from their inherent precision.

As in the preceding section, we once again employ three distinct models combined with a stellar activity prediction to test the structure of the system. Initially, we model the system as comprising three Keplerians, namely b, c, and d, with respective periods of approximately 7, 38, and 151 d. To further evaluate, the presence of the outermost planet and validate the 38-d planet, we also model the RVs with only two Keplerians. The first model includes signals from only planets b and c, while the second model includes signals from only planets b and d.

We use the same pipeline as in Section 7.1 and similar MCMC structure, with 700 chains over 5000 iterations each and a discarded 1000-steps burn-in. We impose priors derived by both the periodogram and the activity proxy GP analysis. Starting with the kernel hyperparameters, we apply an informed uniform prior between 40 and 47 d on the stellar rotational period, P_{rot}, primarily to prevent any signal 'bleeding' between the modelled stellar activity and the Keplerian c, or in other words to prevent the hyperparameter period of the QP kernel from modelling a planetary signal instead of the stellar activity, or from absorbing only part of the periodic signal at this frequency yielding a lower planetary mass than expected. The harmonic complexity μ is constrained with a uniform prior to be between [0,1]. We also impose a uniform prior on the jitter term between [0, 2] m s^{-1}. All prior information for the GP is also included in Table 4.

We then compute the likelihood and the AICc for the three models, as shown in Table 5. Overall, we find no strong statistical preference for one model. We can however reject the model with two-Keplerians (b and c). The logarithm of the likelihood function, $\ln\mathcal{L}$, shows a preference for the model with three Keplerians, reinforcing the long-period signal as a planetary candidate. However, when considering the AICc, which balances the goodness of fit and the complexity of the model, the difference between the AICc of the model with two Keplerians (b and d) and the model with three Keplerians is less than 4, which makes it difficult to differentiate between these two models. The slight preference of the AICc for the two-Keplerians bd model is understandable, considering that the period of Keplerian c is so close to the rotational period of the star. This results in the GP absorbing the signal of the middle Keplerian at 38 d (Damasso et al. 2018). We perform further analyses to fully assess the strength of this third signal around stellar rotation. Finally, taking into consideration the results presented below in Section 7.2.1, alongside the periodogram analysis undertaken in Section 5, we decide to concentrate on and present the three-Keplerian model results.

The final parameters for the three Keplerians and the GP kernel are available in Tables 3 and 4, respectively. The orbital periods of all three Keplerian signals are found to be 7.3, 38, and 151 d and their eccentricities are close to 0. The radial velocity semi-amplitudes for Keplerians b, c, and d are constrained at 13σ, 2σ, and 4σ levels, respectively. When analysing the activity using a GP, we significantly improve the detection of the innermost planetary candidate, even though the constraints on the outer two planets are not as robust. The increased uncertainties in the semi-amplitudes are also reflected in the uncertainties of their masses. Similarly, the GP amplitude is determined to be $3.06^{+0.52}_{-0.36}$ m s^{-1}, with a period of $42.87^{+0.99}_{-1.02}$ d. The outcomes of this model are plotted in Fig. 9, and the phase-folded RVs for all Keplerians can be found in Fig. 10.

7.2.1 Identifying periodic signals at 38 d: planetary candidate or stellar activity?

GLS periodogram tests: To investigate the interaction between the yearly aliasing effect, the Keplerian with a 38-d period, and the stellar rotation signal at 42.6 d, we aimed to reproduce the GLS periodogram for both sinusoidal signals at 42.6 and 38 d. Initially, we simulated a sinusoid with 42.6 d period at the observed epochs, assuming its amplitude to be the GP amplitude derived from the one-dimensional GP analysis in Section 7.2. The resulting GLS periodogram of this simulated data is depicted by the red line in Fig. 11. However, it is evident from the figure that there is insufficient power at the 38-d period compared to the GLS periodogram of the YVA RVs (with stellar activity).

To address this discrepancy, we introduced an additional sine wave at the 38-d period, using the Keplerian parameters of HD48948c, derived from the three-Keplerian model in the one-dimensional GP analysis from Section 7.2. The GLS periodogram of this modified data closely aligns with the YVA radial velocity periodogram,

Table 3. The table displays the results of three Keplerian models, as discussed in Sections 7.1, 7.2, and 7.3. The values and uncertainties of each parameter are derived from their respective posterior distributions, with the 50th percentile representing the central value and the 16th to 84th percentile range indicating 1σ uncertainty. Additionally, the derived parameters, as explained in Section 7.3, are also included in this table. The maximum equilibrium temperature is calculated assuming an albedo (A_B) of 0 and isotropic re-emission and uniform equilibrium temperature.

Parameter	Symbol	Unit	HD48948 b	HD48948 c	HD48948 d
Three Keplerians-only analysis on YV2 RVs					
Orbital period	P	days	$7.33982^{+0.00082}_{-0.00085}$	$37.998^{+0.018}_{-0.019}$	$151.12^{+0.56}_{-0.49}$
RV amplitude	K	$\mathrm{m\,s^{-1}}$	$1.35^{+0.18}_{-0.17}$	$1.71^{+0.20}_{-0.22}$	1.09 ± 0.19
Eccentricity	e		$0.06^{+0.10}_{-0.05}$	$0.06^{+0.09}_{-0.05}$	$0.10^{+0.18}_{-0.09}$
Argument of periastron	ω	rad	$0.83^{+1.27}_{-1.28}$	$-1.06^{+1.24}_{-1.00}$	$-1.02^{+1.43}_{-1.11}$
	$\sqrt{e}\cos\omega$		$0.07^{+0.19}_{-0.16}$	$0.04^{+0.15}_{-0.20}$	$0.04^{+0.17}_{-0.30}$
	$\sqrt{e}\sin\omega$		$0.09^{+0.20}_{-0.15}$	$-0.11^{+0.13}_{-0.19}$	$-0.14^{+0.18}_{-0.27}$
Time of periastron	t_p	BJD	$2456574.05^{+1.53}_{-1.49}$	$2456570.22^{+5.98}_{-7.11}$	$2456564.06^{+18.67}_{-31.89}$
Minimum mass	$m\sin(i)$	$\mathrm{M}_\oplus$	3.18 ± 0.41	$6.97^{+0.82}_{-0.89}$	$6.93^{+1.21}_{-1.24}$
One-dimensional GP analysis on YVA RVs					
Orbital period	P	days	$7.34012^{+0.00052}_{-0.00046}$	$37.99^{+0.16}_{-0.22}$	150.28 ± 0.69
RV amplitude	K	$\mathrm{m\,s^{-1}}$	$2.07^{+0.15}_{-0.17}$	1.06 ± 0.69	$1.55^{+0.35}_{-0.38}$
Eccentricity	e		$0.08^{+0.06}_{-0.05}$	$0.23^{+0.14}_{-0.19}$	$0.15^{+0.17}_{-0.10}$
Argument of periastron	ω	rad	$0.55^{+0.95}_{-0.92}$	$-0.48^{+1.81}_{-1.40}$	$-1.05{-0.79}^{+0.96}$
	$\sqrt{e}\cos\omega$		$0.16^{+0.13}_{-0.18}$	$0.13^{+0.34}_{-0.40}$	$0.10^{+0.20}_{-0.33}$
	$\sqrt{e}\sin\omega$		$0.11^{+0.14}_{-0.18}$	$-0.11^{+0.46}_{-0.33}$	$-0.25^{+0.23}_{-0.20}$
Time of periastron	t_p	BJD	$2456573.74^{+1.05}_{87}$	$2456571.71^{+10.5}_{-9.80}$	2456571.52 ± 15.3
Minimum mass	$m\sin(i)$	$\mathrm{M}_\oplus$	$4.86^{+0.35}_{-0.39}$	$3.94^{+3.02}_{-2.85}$	$9.72^{+2.26}_{-2.56}$
Multidimensional GP analysis on YVA RVs					
Orbital period	P	days	$7.34013^{+0.00040}_{-0.00040}$	$37.920^{+0.026}_{-0.024}$	$150.95^{+0.45}_{-0.41}$
RV amplitude	K	$\mathrm{m\,s^{-1}}$	2.11 ± 0.13	1.75 ± 0.25	1.72 ± 0.22
Eccentricity	e		$0.078^{+0.058}_{-0.050}$	$0.22^{+0.10}_{-0.11}$	$0.12^{+0.12}_{-0.08}$
Argument of periastron	ω	rad	$0.68^{+0.84}_{-0.77}$	$1.76^{+0.66}_{-0.54}$	$4.69^{+1.19}_{-1.21}$
	$\sqrt{e}\cos\omega$		$0.17^{+0.13}_{-0.18}$	$-0.08^{+0.23}_{-0.22}$	0.01 ± 0.24
	$\sqrt{e}\sin\omega$		$0.14^{+0.13}_{-0.17}$	$0.41^{+0.13}_{-0.21}$	$0.21^{+0.25}_{-0.19}$
Time of periastron	t_p	BJD	$2459003.44^{+1.06}_{-0.83}$	$2459019.8^{+3.5}_{-2.7}$	2459107^{+24}_{-42}
Minimum mass	$m\sin(i)$	$\mathrm{M}_\oplus$	4.96 ± 0.32	6.9 ± 1.0	11.0 ± 1.5
TWEAKS **analysis on** TWEAKS **RVS**					
Orbital period	P	days	7.34013 ± 0.00040	38.06 ± 0.06	151.92 ± 0.44
RV amplitude	K	$\mathrm{m\,s^{-1}}$	2.28 ± 0.15	1.48 ± 0.39	1.55 ± 0.34
Eccentricity	e		0.055 ± 0.043	0.55 ± 0.044	0.055 ± 0.044
Argument of periastron	ω	rad	$0.68^{+0.84}_{-0.77}$	$1.76^{+0.66}_{-0.54}$	$4.69^{+1.19}_{-1.21}$
Time of periastron	t_p	BJD	2456567.026 ± 1.72	2456557.14 ± 12.5	2456494.34 ± 20.1
Minimum mass	$m\sin(i)$	$\mathrm{M}_\oplus$	5.43 ± 0.30	6.33 ± 1.6	10.05 ± 2.27
Derived parameters					
Semimajor axis	a	au	0.0652 ± 0.0005	0.1951 ± 0.0016	0.4894 ± 0.0042
Semimajor axis	a	arcsec	0.0039	0.0116	0.0291
Scaled semimajor axis	$a/R_\star$		20.65 ± 0.21	61.79 ± 0.62	154.97 ± 1.61
Incident flux	F_inc	$F_{\mathrm{inc},\oplus}$	138.85 ± 6.98	15.50 ± 0.78	2.46 ± 0.12
Equilibrium temperature	T_eq	K	957 ± 11	553 ± 6	349 ± 4

demonstrating the best match, as illustrated by the solid blue line in Fig. 11. This result provides further supporting evidence for the existence of a periodic signal with a 38-d period, distinct from the stellar rotation signal at 42.6 d.

GP mock data tests: We further evaluate whether it is appropriate to directly compare likelihoods and AICc values for models in scenarios where a planet's orbital period is very similar to the period of a GP. To accomplish this, we take the activity signal that was removed by the YARARA pipeline (i.e. using YVA–YV1 RVs) and inject a Keplerian signal with a 38-d orbital period. Initially, we set the Keplerian semi-amplitude to match the results obtained from the one-dimensional GP analysis for the three-Keplerian model (with a value of K = 1.06 $\mathrm{m\,s^{-1}}$). We also examine extreme cases by testing semi-amplitude values of 1.75 and 0.38 $\mathrm{m\,s^{-1}}$, representing the uncertainties. Subsequently, we perform an analysis to fit these RVs using two distinct models: a GP + Keplerian model that incorporated

Table 4. Stellar activity priors and results from the GP regression analyses undertaken in Sections 7.2 and 7.3 (upper section and lower section). Priors have been identified as follows: $\mathcal{U}$ is a uniform prior.

Parameter	Unit	Prior	Values
One-dimensional GP analysis			
GP amplitude A	$\mathrm{m\,s^{-1}}$	$\mathcal{U}[0, 20]$	$3.06^{+0.52}_{-0.36}$
GP time-scale τ	d	$\mathcal{U}[0, +\infty]$	$110.84^{+29.53}_{-23.23}$
GP period P_{rot}	d	$\mathcal{U}[40, 47]$	$42.87^{+0.99}_{-1.02}$
GP smoothness μ		$\mathcal{U}[0, 1]$	$0.59^{+0.10}_{-0.09}$
Jitter β	$\mathrm{m\,s^{-1}}$	$\mathcal{U}[0, 2]$	$0.84^{+0.11}_{-0.09}$
Multidimensional GP analysis			
GP amplitude V_c	$\mathrm{m\,s^{-1}}$	$\mathcal{U}[0, 20]$	$2.66^{+0.43}_{-0.35}$
GP amplitude V_r	$\mathrm{m\,s^{-1}}$	$\mathcal{U}[-20, 20]$	$9.9^{+2.5}_{-2.2}$
GP time-scale τ	d	$\mathcal{U}[0, 200]$	$96.8^{+12}_{-6.7}$
GP period P_{rot}	d	$\mathcal{U}[35, 50]$	$43.45^{+1.00}_{-0.71}$
GP smoothness μ^a		$\mathcal{U}[0.0, 1.0]$	$0.75^{+0.11}_{-0.09}$
Jitter β	$\mathrm{m\,s^{-1}}$	$\mathcal{U}[0.0, 5.0]$	$0.89^{+0.09}_{-0.08}$

[a] To allow for a direct comparison, we already included the conversion factor resulting from the different definitions of the parameter.

Table 5. Likelihood and AICc comparison between the tested models (3 Keplerians bcd, 2 Keplerians bc, 2 Keplerians bd) in Sections 7.1, 7.2, and 7.3. The models highlighted in bold are the most favoured in each analysis based on their likelihood and AICc.

Parameter	3 Keplerians bcd	2 Keplerians bc	2 Keplerians bd
Keplerian-only analysis			
$\ln \mathcal{L}$	− 379.89	−482.17	−550.62
AICc	792.55	985.58	1122.48
One-dimensional GP analysis			
$\ln \mathcal{L}$	− 350.95	−361.28	−352.66
AICc	746.90	755.33	738.07
Multi-dimensional GP analysis			
$\ln \mathcal{L}$	− 167.0	−179.1	−173.5
AICc	370.3	388.5	376.5

both an activity term (using a quasi-periodic kernel) and a Keplerian signal with a 38-d period (as expected in the generated data set), and a GP-only model that included only the activity component. In all three runs that included the Keplerian signal, we successfully recover the injected Keplerian parameters. The semi-amplitudes of the Keplerians for the three cases (0.38, 1.06, and 1.75 $\mathrm{m\,s^{-1}}$) show consistency within 1σ and are determined to be $0.47^{+0.37}_{-0.32}$ $\mathrm{m\,s^{-1}}$, $1.12^{+0.33}_{-0.45}$ $\mathrm{m\,s^{-1}}$, and $1.87^{+0.28}_{-0.31}$ $\mathrm{m\,s^{-1}}$, respectively. Additionally, the parameters for the GP, including period and amplitude, are found to be consistent within 1σ uncertainties amongst the three runs.

We then examined the likelihoods and AICc values, which are detailed in the Appendix in Table A1. When comparing runs with and without the Keplerian signal, we observe that the AICc strongly favored the GP-only approach in the case with the lowest injected semi-amplitude of 0.38 $\mathrm{m\,s^{-1}}$. For the intermediate semi-amplitude level (1.06 $\mathrm{m\,s^{-1}}$), we could distinguish between the GP-only and GP+Keplerian models with 95 per cent confidence. Finally, we find that the GP+Keplerian model was more suitable in the case with the highest semi-amplitude of 1.75 $\mathrm{m\,s^{-1}}$, where the Keplerian signal was most prominent. These findings indicate that when Keplerian orbital periods closely match the activity period, a GP analysis can effectively absorb the Keplerian signal within the activity signal (Damasso et al. 2018). This explains the slight preference for the two-Keplerian model (b and d) over the three-Keplerian model, as described in Section 7.2. Therefore, it is important to exercise caution and take into account the astrophysical context when interpreting AICc comparisons in such situations.

7.3 Multidimensional GP analysis

We employ the GP framework introduced by Rajpaul et al. (2015), also commonly known as multidimensional GP, to simultaneously model the RVs, the BIS, and the log R'_{HK}. For this analysis, we use the YARARA RVs with the reinjected stellar activity signal (YVA), following the prescriptions of Stalport et al. (2023). The kernel of choice for the underlying GP is again the quasi-periodic one, in the mathematical formulation of Grunblatt, Howard & Haywood (2015)[4], and implemented in PYORBIT[5] (Malavolta et al. 2016, 2018) through the library TINYGP[6] for improved performances (see also Nardiello et al. 2022 and Mantovan et al. 2024). For all the data sets, we include a convective blueshift suppression term, which is a close proxy for the fractional coverage of active regions, and is related to the underlying GP through the amplitudes V_c, B_c, L_c for the YVA RVs, BIS, and log R'_{HK}, respectively. For the RVs and BIS only, we include an additional term related to the RV of the stellar surface at the location of the activity regions, approximated with the first derivative of the underlying GP, and tied to the observations through the amplitude V_r and B_r (Aigrain, Pont & Zucker 2012; Rajpaul et al. 2015). It is worth noting that we had the option to substitute the log R'_{HK} with the FWHM, given that both are dependent solely on the convective blueshift suppression term. However, due to the close resemblance between the two time series (refer to Section 6 and Fig. 6), we anticipate minimal improvement by incorporating or substituting the former with the latter. Instead, the inclusion of BIS becomes essential, despite its weaker correlation with RV. This is necessary because we require at least one data set sensitive to the rotational modulation of the active regions, other than the RV themselves, to constrain the first derivative of the underlying GP.

In principle, the multidimensional GP should be able to disentangle planetary and activity signals even when the corresponding time-scales are close, as the modelling across multiple activity-only time series should prevent the GP from *absorbing* the planet signal (e.g. Rajpaul et al. 2021). To test this thesis, we deliberately enlarge the boundaries of the rotational period of the star to include the orbital period of Keplerian c, without providing any Gaussian prior on the hyperparameters of the GP or the jitter parameters of the data sets (see Table 4). For the orbital period of the Keplerians, we impose uniform priors in the range of [3, 10], [10, 100], and [100, 300] d for Keplerians b, c, and d, respectively, while the orbital phase of each Keplerian is parametrized as the sum of the argument of pericenter ω and the mean anomaly M_0 at the arbitrary reference time $T_{\mathrm{ref}} = 2459000.0$ (Ford 2006). Except for these differences, the modelling of the Keplerian signals is consistent with the analysis reported in Sections 7.1 and 7.2. Fig. A1 displays the YVA RVs, BIS, and log R'_{HK} time series alongside the best-fitting model. For a closer view focusing on the last semester of data and highlighting the

---

[4] The only difference with equation (4) is a $\sqrt{2}$ factor in the definition of the coherence scale parameter.

[5] https://github.com/LucaMalavolta/PyORBIT, version 10.

[6] https://github.com/dfm/tinygp

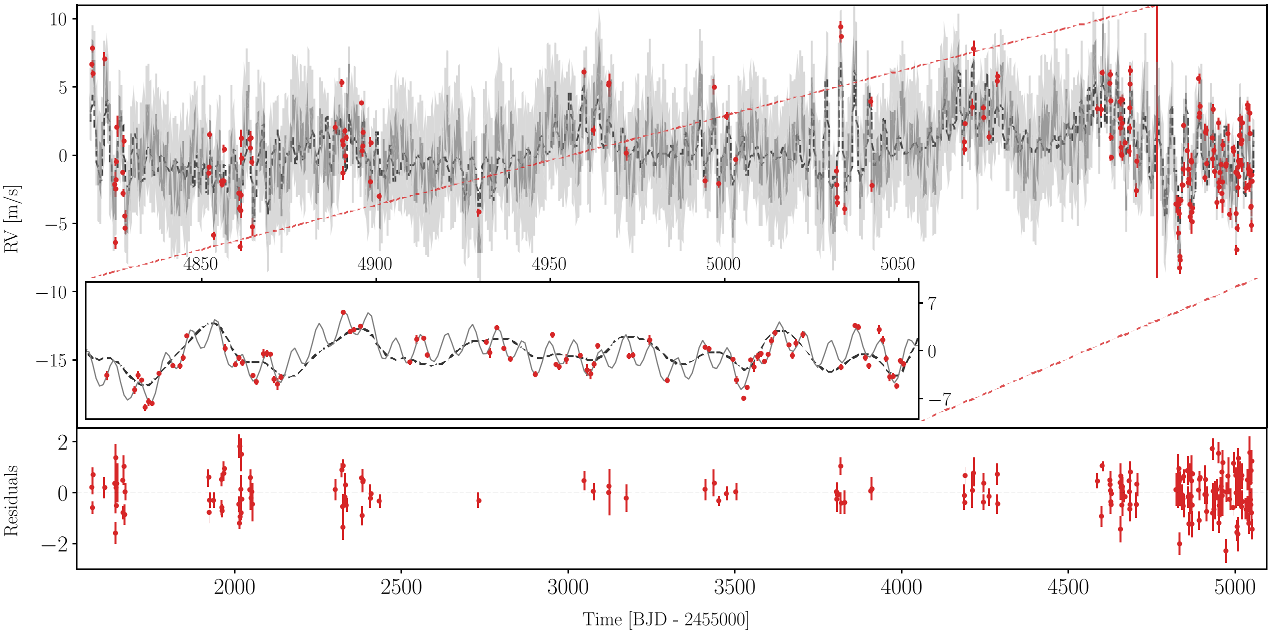

Figure 9. Top panel: The figure illustrates the YVA RVs of HD 48 948 in solid red circles. The complete model from the one-dimensional GP analysis, which includes three Keplerians and expected stellar activity, is represented by a grey line. The grey-shaded area indicates the model's uncertainties. A zoomed-in version of the last semester of data is also provided, with the modelled activity shown as a black dashed line, revealing a recurring pattern. Bottom panel: The residuals, or the differences between the radial velocity and the model (grey line), are plotted at the bottom.

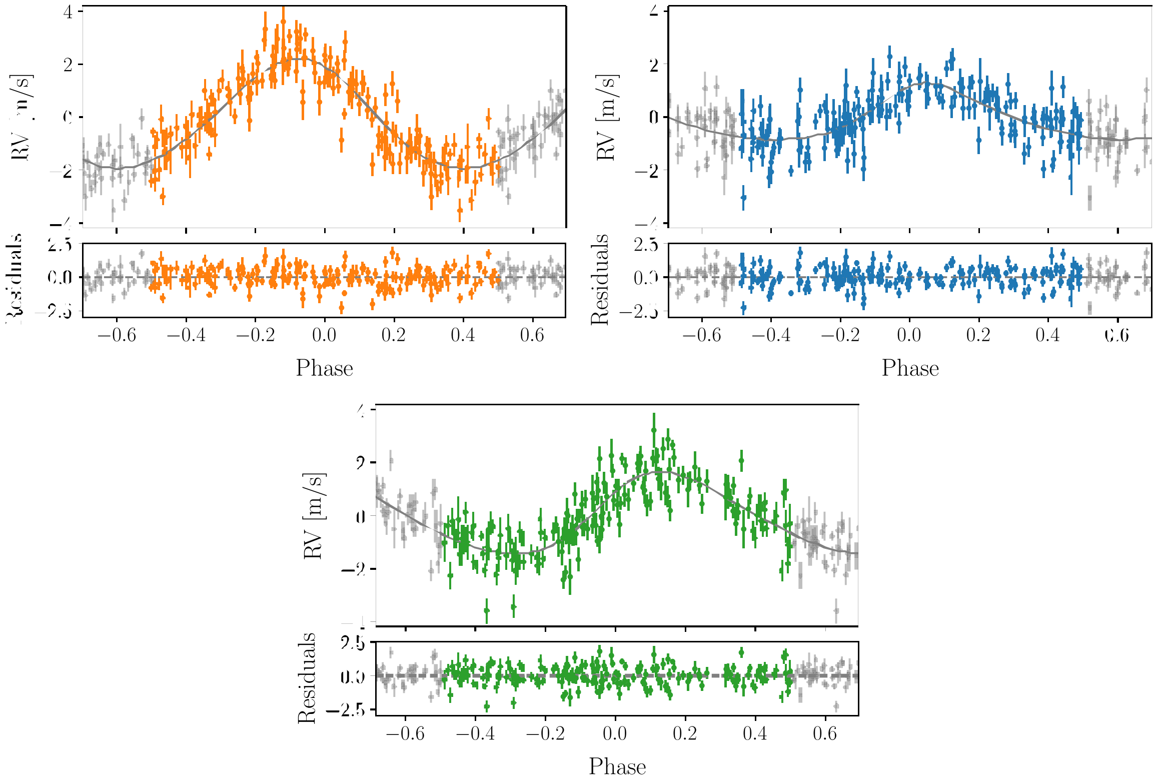

Figure 10. *Phase folded plots:* The figure shows the phase folded YVA RVs of HD 48 948 at periods of 7.3, 38, and 151 d, represented by orange, blue, and green data points, respectively. The best-fitting model from the one-dimensional GP run is depicted by the grey line in each plot. In all figures, the signal originating from other Keplerians and stellar activity (GP) has been removed from both the grey line and the RVs.

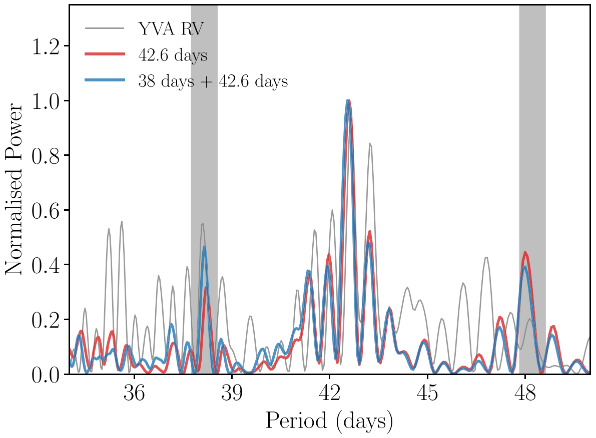

Figure 11. The GLS periodogram of YARARA VA RVs is represented by a grey line, which reveals significant power at a period of 42.6 d. The red line illustrates the periodogram of the sinusoidal signal that corresponds to the stellar rotation period of 42.6 d. The blue line represents the GLS periodogram of the two sinusoidal signals at periods of 42.6 and 38 d. The shaded grey areas indicate the 1-yr alias for the 42.6-d period.

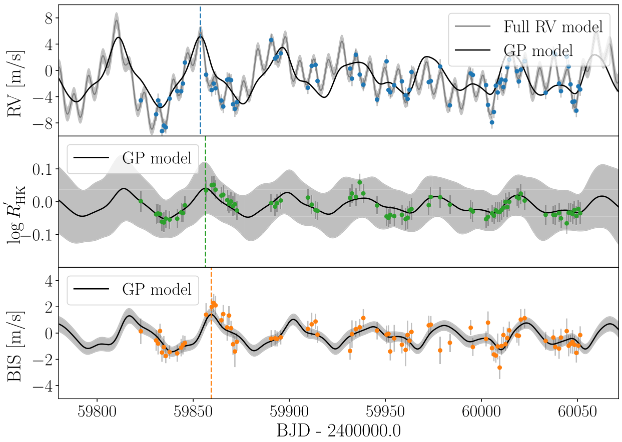

Figure 12. *Multidimensional GP*: The figure shows the zoomed-in version of the last semester of data and the best-fitting model from the multidimensional GP regression. The black line in all plots represents the modelled activity, revealing a recurring pattern while the grey line in the YVA RVs (top panel) shows the modelled activity combined with the three Keplerian model. The dashed blue, green, and orange line represents the maxima of corresponding peaks, indicating a time lag between RVs and activity indicators (log $R'_{\rm HK}$ and BIS).

model as well as the lag between RVs and activity indicators, refer to the zoomed-in version presented in Fig. 12.

The main results of our analysis are reported in Tables 3 and 4. Compared to the use of Keplerian-only and one-dimensional GP analyses, we recover the RV semi-amplitude of the three Keplerian signals with a semi-amplitude significance of better than 7σ. At the same time, all the orbital values are consistent with the previous analysis. The stellar rotation period and the orbital period of Keplerian *c* are well disentangled, being $P_{\rm rot} = 43.45^{+1.00}_{-0.71}$ d and $P_{\rm c} = 37.92 \pm 0.03$ d, despite our lack of attempts to avoid any bleeding in the frequency space. Consistently with the previous analyses, we compute the AICc for models encompassing either Keplerians *b* and *c*, or *b* and *d*, in addition to the three-Keplerian model already presented. When considering multidimensional GP in our analysis, the three-Keplerian model is clearly preferred over the other models, with ΔAICc = 18.2 for two-Keplerian (b and c) and ΔAICc = 6.2 for two-Keplerian (b and d). The log-likelihood and AICc of the tested models are reported in 5. Note, however, that the results of the multidimensional GP analysis cannot be compared directly with the other results in the table as we used a different number of data sets. The addition of a fourth Keplerian with orbital period bounded between 3 and 1000 d resulted in a non-detection, with ΔAICc = 39 in favour of the three-planet model. The resulting semi-amplitudes for the Keplerians are $K_{\rm b} = 2.11 \pm 0.13$ m s^{-1}(16σ), $K_{\rm c} = 1.75 \pm 0.25$ m s^{-1}(7σ), $K_{\rm d} = 1.72 \pm 0.22$m s^{-1}($8\sigma$), corresponding to the minimum masses of $m_{\rm b} = 4.96 \pm 0.32$ M$_\oplus$, $m_{\rm c} = 6.9 \pm 1.0$ M$_\oplus$, and $m_{\rm d} = 11.0 \pm 1.5$ M$_\oplus$.

8 INDEPENDENT ANALYSIS USING TWEAKS

The CCFs obtained from the HARPS-N DRS were independently examined for planetary signals using TWEAKS (Anna John, Collier Cameron & Wilson 2022; Anna John et al. 2023). This pipeline was specially designed to achieve a sub-m s^{-1} detection threshold at extended orbital periods by integrating the wavelength-domain and time-domain stellar activity mitigation (Anna John et al. 2023). We also observe particular instrumental systematics in TWEAKS RVs occurring during periods of instrument defocusing, as shown in Fig. 2.

We start with a blind search of RVs, using a model with up to five undetected Keplerian signals. We utilize the KIMA nested-sampling package (Faria et al. 2018) to do this. Time-domain activity-decorrelation vectors (a.k.a basis vectors) are generated using SCALPELS (Collier Cameron et al. 2021), which does a principal-component analysis on the autocorrelation function of the CCF. These basis vectors are then used for the spectral line-shape decorrelation in KIMA, as Anna John et al. (2022) observed that detrending the RVs for line shape variations using the SCALPELS basis vectors yields a model that is considerably better than a model that neglects to account for these stellar activity signatures.

The joint posteriors clearly detect two Keplerian signals at orbital periods 7.3401 ± 0.0004 and 38.01 ± 0.06 d. However, we observe an instrumental systematic that is possibly giving rise to spurious signals at periods greater than 300 d. To test this systematic, we perform an additional analysis in which we limit the orbital period for the search for Keplerians to 270 d to prevent any long-term systematic from potentially interfering with and influencing any other legitimate Keplerian signals. This analysis discloses the existence of a third planetary candidate on an orbit spanning 150.98 ± 0.77 d, without compromising the detection precision of the two inner planetary candidates, as shown in Fig. 13. We also confirm the coherency of the signals across different data subsets to validate these findings, as in Anna John et al. (2023). In contrast to signals caused by sampling patterns, stellar activity, or aliases, the 7.34 and 37.98-d signals were identified in all subsets with $\sigma \geq 5$.

To search for numerous Keplerian signals simultaneously and verify their detection significance, we perform a False Inclusion Probability (FIP) analysis (Hara et al. 2022) in frequency space, with the bin size set to the Nyquist frequency resolution for the whole data duration. The 7.3, 38, and 151 d periodicities appear to have the lowest FIPs, closer to zero, as can be seen in the bottom panel of Fig. 13, as would be expected for any strong and coherent planetary signal. We then performed a Gaussian Mixture modelling to the posteriors Anna John et al. (2023) to obtain the orbital parameters. The resulting RV semi-amplitudes for signals at 7.3, 38, and 151 d are 2.29 ± 0.13 (18σ), 1.48 ± 0.39 m s^{-1}(4σ), and

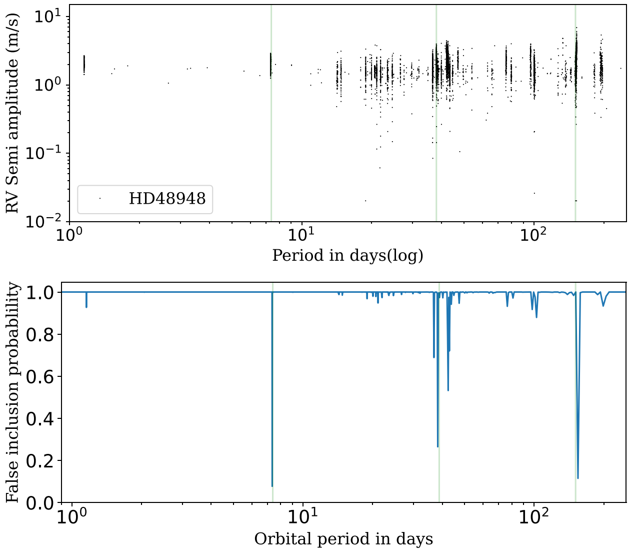

Figure 13. Results from the TWEAKS pipeline. Top: posterior distribution. Bottom: False Inclusion Probability (FIP) periodogram. The vertical plain lines (light green) depict the three planet detections with significant FIPs at 7.34, 37.98, and 150.92 d, respectively. The clustering around the 37.98 d planet signal can be attributed to the stellar rotation period and its 1 yr aliases.

1.55 ± 0.34 m s^{-1}(5σ), respectively. Incorporating the stellar mass of 0.686 $M_\odot$ to calculate the minimum masses, we determine the masses of planetary candidates to be 5.43 ± 0.30, 6.33 ± 1.61, and 10.05 ± 2.27 $M_\oplus$, respectively. The final parameters for the three Keplerians are reported in Table 3.

9 COMPARATIVE ANALYSIS AND AVERAGE KEPLERIAN PARAMETERS

In this section, we examine the outcomes derived from different analyses of the three data sets. In each analysis, we identify three Keplerians with orbital periods of 7.3, 38, and 151 d.

In the case of YV2 RVs, we observe smaller Keplerian amplitudes leading to smaller masses. So, we further analyse the YV2 data to understand the reasons behind the slight reduction in Keplerian amplitudes after YARARA processing. Initially, we ruled out the possibility of absorption by YV2, considering that the planets were included in the fitted model. This raised concerns about the YARARA correction of the spectra. YARARA primarily focuses on detecting new planetary signals obscured by radial velocity contamination.[7] However, accurate masses can be obtained in a second iteration by including a Keplerian solution during spectra pre-processing (see section 2.1 in Cretignier et al. 2021). Initially such analysis was implemented to eliminate binary and large planetary signals, but it is also crucial for recovering accurate masses. The updated masses of three planets from the second iteration of YV2 data are $4.26^{+0.45}_{-0.42}$ $M_\oplus$for 7.3 d candidate, $8.57^{+0.83}_{-0.98}$ $M_\oplus$ for 38 d candidate, and $10.73^{+1.21}_{-1.32}$ $M_\oplus$ for 151 d candidate. We show in Fig. 14 that the masses obtained by YV2 (after the second iteration of the code) are compatible with the other methods.

We observe a slight variation in the mass estimate for Keplerian c with a 38-d orbital period, particularly as it is close to the stellar rotation period. Specifically, YV2 results in a somewhat higher mass compared to YVA or TWEAKS. This discrepancy may stem from the fact that YV2 attempts to directly correct for activity in the spectra rather than in the time domain.[8] This suggests that either methods fitting in the time domain partially absorb the planetary signal amplitude, or that activity signals are still present in YV2, thereby enhancing the planetary amplitudes. In either case, obtaining an accurate mass for a planet situated so close to the rotational period proves to be a challenging task.

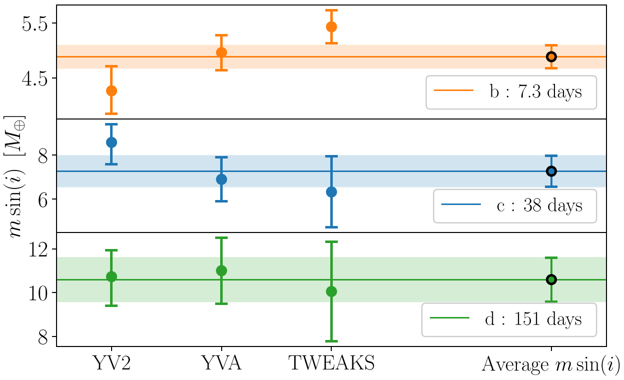

Figure 14. The figure shows the minimum masses of three Keplerians obtained from different data sets, with the average mass of all three presented on the right. The shaded region shows the uncertainty on the average minimum mass.

Given the inherent limitations and advantages associated with various radial velocity (RV) data sets and analyses, we determine an average of minimum mass and its corresponding uncertainty for each planetary candidate across different RV data sets (YV2, YVA, TWEAKS). For YVA RVs, we use the minimum mass obtained from the multidimensional GP regression. We find that the minimum masses of the planetary candidates are 4.88 ± 0.21, 7.27 ± 0.70, and 10.59 ± 1.00 $M_\oplus$, respectively. Additionally, the results from all analyses fall within 1σ of the average minimum mass.

We also compute the incident flux, $F_{\rm inc}$, of these three planetary candidates in terms of the incident flux received by Earth from the Sun, $F_{\rm inc,\oplus}$, following the formula:

$$\frac{F_{\rm inc}}{F_{\rm inc,\oplus}} = \left(\frac{T_{\rm eff}}{\rm T_\odot}\right)^4 \left(\frac{R_\star}{\rm R_\odot}\right)^2 \left(\frac{1}{a}\right)^2, \tag{5}$$

where $T_{\rm eff}$ is the stellar effective temperature, $R_\star$ is the stellar radius, and a is the semimajor axis of the planet. We then calculate the equilibrium temperatures of the three planetary candidates $T_{\rm eq}$ using

$$T_{\rm eq} = T_{\rm eff}\sqrt{\frac{R_\star}{2a}}[f(1 - A_B)]^{1/4}, \tag{6}$$

where f is the effectiveness of atmospheric circulation and $A_{\rm B}$ is the Bond albedo. For simplicity, we assume isotropic re-emission and uniform equilibrium temperature over the entire planet, setting $f = 1$, and black-body absorption, setting $A_{\rm B} = 0$, and derive the upper limit of $T_{\rm eq}$. The calculated $F_{\rm inc}$ and maximum equilibrium temperatures for HD48948 b, c, and d are included in Table 3. Finally, we determine the habitable zone around the star by employing models that compute the inner and outer boundaries of this zone based on

---

[7] To this regard, YARARA was successful in revealing candidates during a preliminary 2021 analysis, its main objective is not precise mass determination.

[8] Although YV2 includes time-domain corrections like SHELL, the limited SNR of the observations makes extracting time-domain proxies more challenging.

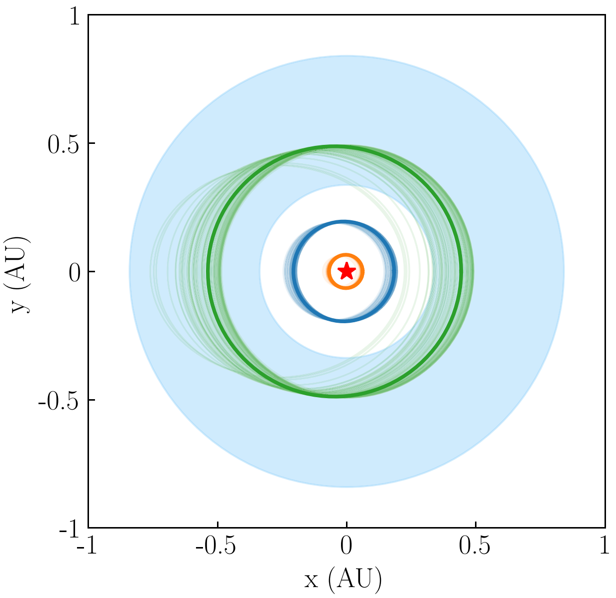

Figure 15. *The HD 48 948 system configuration:* The inner planetary candidates, depicted in orange and blue, have circular orbits of 7.3 and 38 d, respectively. The outer planetary candidate, illustrated in green, has an orbit of 151 d. A selection of 100 random orbits from the MCMC chains for each of the three planetary candidate are represented in lighter shades. The habitable zone boundaries, shown as sky-blue shaded regions, are calculated as outlined in Section 8.2, based on the findings of Kopparapu et al. (2013).

the Recent Venus and Early Mars model, as detailed in Kopparapu et al. (2013).

10 RESULTS AND DISCUSSION

As part of the HARPS-N RPS programme, we study HD 48948, a moderately active a bright K-dwarf star located 16.8 parsecs away. We analyse the high-precision RV measurements from the HARPS-N spectrograph. To ensure the robustness of our findings, we employed multiple methods to extract RVs from the spectra (YV2, YVA, TWEAKS) and utilized various analyses involving only Keplerians, 1D GP regression (1D GP), and multi-GP regression (multi-GP) to analyse the data and finally compare their results. We summarize our results below:

(i) *Discovery of three planetary candidates:* After careful analysis of the RVs and activity indicators, we report the discovery of three low-mass planetary candidates orbiting HD 48948.

(ii) *Orbital parameters:* We find three planetary candidates with orbital periods of 7.3, 38, and 151 d, and with minimum masses of 4.88 ± 0.21, 7.27 ± 0.70, and 10.59 ± 1.00 $M_\oplus$, respectively. All the planetary candidates have low eccentricities.

(iii) *HD 48 948 configuration*: Fig. 15 shows the arrangement of the planetary candidates around HD 48 948 with the habitable zone represented by the sky-blue circular ring. In particular, we find that HD 48 498 d is located in the habitable zone of the star. It is a promising target for future high-contrast direct imaging and high-resolution spectroscopic studies with a separation of 0.029 arcsec from its star.

(iv) *Complexity in stellar variability modelling:* The presence of stellar activity complicates the analysis of these data sets. Even though we employed different data reduction methods, it was still not possible to completely eliminate or accurately model the variability of the star. As a result, it is very challenging to determine accurate and precise masses of the super-Earth candidates, including the super-Earth candidate within the habitable zone. This emphasizes the importance of improving the understanding of stellar variability prior to embarking on surveys to detect low-mass planets with moderate to long orbital periods.

10.1 Limits on outer companions

No detectable astrometric acceleration is measured for HD 48 948 in the Brandt (2021) and Kervella, Arenou & Thévenin (2022) catalogues. The limits on the presence of planetary mass companions placed by the technique are however rather interesting. In Fig. A2, we show the sensitivity curve obtained based on the analytical formulation of Kervella et al. (2019). As we can see, Saturn-mass companions are ruled out in the approximate separation range 3–10 au. This system is a relevant addition to the sample of compact small-mass multiples with no detected outer gas giants which have been the subject of a growing body of recent studies on the relative occurrence of close-in small planet systems with and without the presence of outer giant planetary companions (e.g. Zhu & Wu 2018; Bryan et al. 2019; Rosenthal et al. 2022; Bonomo et al. 2023; Pinamonti et al. 2023; Weiss et al. 2024).

11 CONCLUSION

11.1 Challenges in data analysis

The analysis of HD 48948's existing data sampling has presented challenges. The complexity arises from the difficulty in distinguishing between the model with three Keplerians and two Keplerians. This challenge is the result of the interaction of the 38-d Keplerian signal with the 42.6 d stellar rotation period, further complicated by the 1-yr alias of stellar rotation. Our analysis emphasizes the significance of actively monitoring rotational modulation signals in every season for active stars, requiring the implementation of effective modeling techniques with Gaussian Processs. Moreover, good data sampling for such stars is essential for the detection of lower mass planets with moderate to long orbital periods. Masses typically remain within a 1σ range despite methodological differences.

11.2 Methodological difference in mass estimation

Fig. 14 displays the minimum masses of the three candidates, highlighting the diverse levels of accuracy and precision in mass determination stemming from discrepancies in our data analysis techniques. While RV data obtained from YARARA may provide better correction of instrumental systematics compared to TWEAKS RVs, it could potentially absorb certain long-term signals. Similarly, GP regression (both 1D and multi-GP) offers a robust mechanism for addressing stellar variability signals in our data set, but it also carries the risk of assimilating signals aligned with the stellar rotation period. These factors directly influence the accuracy and precision in determining the mass of the planet. The challenge of identifying the most dependable method for handling stellar variability and instrumental systematics remains significant. Extensive investigations involving a broader array of stars are necessary for generalization and for determining the optimal approach.

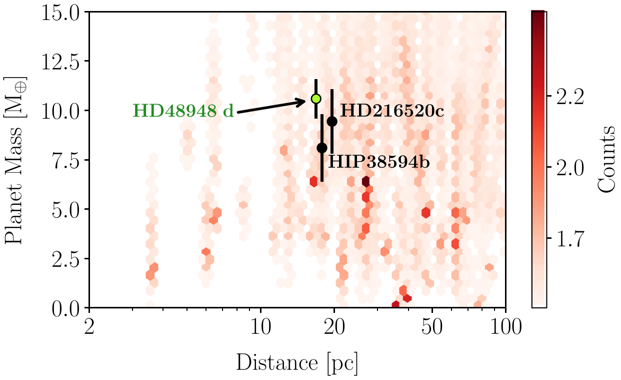

Figure 16. *Planetary mass versus distance from Earth*: A two-dimensional binned density plot in redscale is used to depict the exoplanets around FGK stars with mass or minimum mass measurements and located within 100 parsecs of our Solar system. The black solid circles represent exoplanets that are within 20 parsecs of Earth, situated in their stars' Habitable Zone, and have a true or minimum mass < 11 $M_{\oplus}$.

11.3 Potential target for direct imaging surveys

The star HD 48948, situated at 16.8 parsecs away from the Solar system, emerges as an exciting target for future high-contrast direct imaging and high-resolution spectroscopic studies. Among its planetary candidates, HD 48 948 d with a minimal angular separation of 0.029 arcsec from its host star, has an effective temperature of 349 K (see Section 10). It stands within detectable range for the Thirty Meter Telescope (TMT; p. 193 from TMT Detailed Science Case: 2022), which is designed to probe smaller separation systems (approximately 0.02°0.1″). The distinctive characteristics and close proximity of HD 48 948 render it a highly promising candidate for not only for the TMT but also for NASA's Habitable Worlds Observatory (HWO), which merges the capabilities of the Large UV/Optical/IR Surveyor (LUVOIR; The LUVOIR Team 2019) and the Habitable Exoplanet Observatory (HabEx; Gaudi et al. 2020).

Fig. 16 shows a two-dimensional binned density plot of exoplanets with mass or minimum mass < 11 $M_{\oplus}$ situated within 100 parsecs around FGK stars (Credits: Data from NASA Exoplanet Archive, available at https://exoplanetarchive.ipac.caltech.edu). In the figure, planets are represented as probability density distributions rather than single points. For each planet, we randomly sampled 1000 points from a Gaussian distribution centred around the planet's mass and stellar distance measurements and the width of the distribution was determined by their respective $1-\sigma$ uncertainties. The resulting distributions are depicted in a two-dimensional binned density plot, where darker regions signify higher counts of such points. Notably, we excluded TAU CET e from the figure due to its nearly pole-on orientation (Korolik et al. 2023). Additionally, HD 40 307 g was excluded the analysis in Unger et al. (2020) does not support the existence of planet g. In the Fig. 16, there are only three candidates around FGK stars that are in the habitable of their star, marked by black solid circles. This places HD 48 948 d as the nearest super-Earth orbiting an K star within the habitable zone.

ACKNOWLEDGEMENTS

The HARPS-N project was funded by the Prodex Program of the Swiss Space Office (SSO), the Harvard University Origin of Life Initiative (HUOLI), the Scottish Universities Physics Alliance (SUPA), the University of Geneva, the Smithsonian Astrophysical Observatory (SAO), the Italian National Astrophysical Institute (INAF), University of St. Andrews, Queen's University Belfast, and University of Edinburgh.

SD acknowledges support from the STFC consolidated grant no. ST/V000721/1. FR is funded by the University of Exeter's College of Engineering, Maths and Physical Sciences, UK. ACC acknowledges support from STFC consolidated grant numbers ST/R000824/1 and ST/V000861/1, and UKSA grant no. ST/R003203/1. KR is grateful for support from UK STFC via consolidated grant no. ST/V000594/1. RDH is funded by the UK Science and Technology Facilities Council (STFC)'s Ernest Rutherford Fellowship (grant number ST/V004735/1). MC acknowledges the SNSF support under grant P500PT_211024. AS, ASB, and MD gratefully acknowledge support from the 'Programma di Ricerca Fondamentale INAF 2023' of the National Institute of Astrophysics (Large Grant 2023 EXODEMO). MP acknowledges support from the Italian Space Agency (ASI) under contract 2018-24-HH.0 'The Italian participation to the Gaia Data Processing and Analysis Consortium (DPAC)' in collaboration with the Italian National Institute of Astrophysics. MP also acknowledges support from the European Union – NextGenerationEU (PRIN MUR 2022 20229R43BH) and the 'Programma di Ricerca Fondamentale INAF 2023'. FPE and CLO would like to acknowledge the Swiss National Science Foundation (SNSF) for supporting research with HARPS-N through the SNSF grant numbers 140649, 152721, 166227, 184618, and 215190. The HARPS-N Instrument Project was partially funded through the Swiss ESA-PRODEX Programme.

This work has made use of data from the European Space Agency (ESA) mission *Gaia* (https://www.cosmos.esa.int/gaia), processed by the *Gaia* Data Processing and Analysis Consortium (DPAC; https://www.cosmos.esa.int/web/gaia/dpac/consortium). Funding for the DPAC has been provided by national institutions, in particular the institutions participating in the *Gaia* Multilateral Agreement. For the purpose of open access, the author has applied a 'Creative Commons Attribution (CC BY) licence to any Author Accepted Manuscript version arising from this submission.

We would like to thank Dr Eduardo Vitral and Dr Tyler Gardner for many valuable comments.

DATA AVAILABILITY

The research data supporting this publication (data products derived from HARPS-N) are openly available as supplementary material.

REFERENCES

Aigrain S., Pont F., Zucker S., 2012, MNRAS, 419, 3147
Akaike H., 1983, 44, 277
Andreasen D. T. et al., 2017, AAP, 600, A69
Anna John A., Collier Cameron A., Wilson T. G., 2022, MNRAS, 515, 3975
Anna John A. et al., 2023, MNRAS, 525, 1687
Baranne A. et al., 1996, A&AS, 119, 373
Barros S. C. C., Demangeon O., Díaz R. F., Cabrera J., Santos N. C., Faria J. P., Pereira F., 2020, A&A, 634, A75
Basri G., Wilcots E., Stout N., 1989, PASP, 101, 528
Benz W. et al., 2021, Exp. Astron., 51, 109
Bonomo A. S. et al., 2019, Nat. Astron., 3, 416
Bonomo A. S. et al., 2023, A&A, 677, A33
Borucki W. J. et al., 2010, Science, 327, 977
Bouchy F., Pepe F., Queloz D., 2001, AAP, 374, 733
Bourrier V. et al., 2021, A&A, 654, A152
Brandt T. D., 2021, ApJS, 254, 42
Bryan M. L., Knutson H. A., Lee E. J., Fulton B. J., Batygin K., Ngo H., Meshkat T., 2019, AJ, 157, 52

Buchhave L. A. et al., 2012, Nature, 486, 375

Burnham K., Anderson D., 2002, Model Selection and Multimodel Inference: A Practical Information-theoretic Approach. Springer Verlag

Chaplin W. J., Cegla H. M., Watson C. A., Davies G. R., Ball W. H., 2019, AJ, 157, 163

Cloutier R. et al., 2020, AJ, 160, 3

Collier Cameron A. et al., 2021, MNRAS, 505, 1699

Cosentino R. et al., 2012, in McLean I. S., Ramsay S. K., Takami H., eds, Proc. SPIE Conf. Ser. Vol. 8446, Ground-based and Airborne Instrumentation for Astronomy IV. SPIE, Bellingham, p. 84461V

Cosentino R. et al., 2014, in Ramsay S. K., McLean I. S., Takami H., eds, Proc. SPIE Conf. Ser. Vol. 9147, Ground-based and Airborne Instrumentation for Astronomy V. SPIE, Bellingham, p. 91478C

Crass J. et al., 2021, preprint (arXiv:2107.14291)

Cretignier M., Dumusque X., Allart R., Pepe F., Lovis C., 2020a, AAP, 633, A76

Cretignier M., Francfort J., Dumusque X., Allart R., Pepe F., 2020b, AAP, 640, A42

Cretignier M., Dumusque X., Hara N. C., Pepe F., 2021, AAP, 653, A43

Cretignier M., Dumusque X., Pepe F., 2022, A&A, 659, A68

Cretignier M., Dumusque X., Aigrain S., Pepe F., 2023, A&A, 678, A2

Cutri R. M. et al., 2013, Explanatory Supplement to the AllWISE Data Release Products. Available at:https://ui.adsabs.harvard.edu/abs/2013wise.rept....1C

Damasso M. et al., 2018, A&A, 615, A69

DiTomasso V. et al., 2023, AJ, 165, 38

Dotter A., 2016, ApJS, 222, 8

Dumusque X., 2018, A&A, 620, A47

Dumusque X., Udry S., Lovis C., Santos N. C., Monteiro M. J. P. F. G., 2011, A&A, 525, A140

Dumusque X. et al., 2012, Nature, 491, 207

Dumusque X. et al., 2021, A&A, 648, A103

Eastman J., Gaudi B. S., Agol E., 2013, PASP, 125, 83

Faria J. P., Santos N. C., Figueira P., Brewer B. J., 2018, J. Open Source Softw., 3, 487

Ford E. B., 2006, ApJ, 642, 505

Fulton B. J. et al., 2017, AJ, 154, 109

Gaia Collaboration, 2023, A&A, 674, A1

Gaudi B. S. et al., 2020, preprint (arXiv:2001.06683)

Grieves N. et al., 2018, MNRAS, 481, 3244

Grunblatt S. K., Howard A. W., Haywood R. D., 2015, ApJ, 808, 127

Hara N. C., Boué G., Laskar J., Correia A. C. M., 2017, MNRAS, 464, 1220

Hara N. C., Delisle J.-B., Unger N., Dumusque X., 2022, A&A, 658, A177

Hatzes A. P., 2013, ApJ, 770, 133

Haywood R. D. et al., 2014, MNRAS, 443, 2517

Howell S. B. et al., 2014, PASP, 126, 398

Kervella P., Arenou F., Mignard F., Thévenin F., 2019, A&A, 623, A72

Kervella P., Arenou F., Thévenin F., 2022, A&A, 657, A7

Kopparapu R. K. et al., 2013, ApJ, 765, 131

Korolik M. et al., 2023, AJ, 166, 123

Lacedelli G. et al., 2021, MNRAS, 501, 4148

Lafarga M. et al., 2020, A&A, 636, A36

Malavolta L. et al., 2016, A&A, 588, A118

Malavolta L., Lovis C., Pepe F., Sneden C., Udry S., 2017, MNRAS, 469, 3965

Malavolta L. et al., 2018, AJ, 155, 107

Mamajek E. E., Hillenbrand L. A., 2008, ApJ, 687, 1264

Mantovan G. et al., 2024, A&A, 682, A129

Mortier A., Collier Cameron A., 2017, A&A, 601, A110

Mortier A., Sousa S. G., Adibekyan V. Z., Brandão I. M., Santos N. C., 2014, AAP, 572, A95

Mortier A. et al., 2020, MNRAS, 499, 5004

Morton T. D., 2015, Astrophysics Source Code Library, record ascl:1503.01

Motalebi F. et al., 2015, A&A, 584, A72

Nardiello D. et al., 2022, A&A, 664, A163

Nicholson B. A., Aigrain S., 2022, MNRAS, 515, 5251

Pepe F. et al., 2002, Messenger, 110, 9

Pinamonti M. et al., 2023, A&A, 677, A122

Rajpaul V., Aigrain S., Osborne M. A., Reece S., Roberts S., 2015, MNRAS, 452, 2269

Rajpaul V., Aigrain S., Roberts S., 2016, MNRAS, 456, L6

Rajpaul V., Buchhave L. A., Aigrain S., 2017, MNRAS, 471, L125

Rajpaul V. M. et al., 2021, MNRAS, 507, 1847

Rescigno F. et al., 2023a, preprint (arXiv:2310.13623)

Rescigno F., Dixon B., Haywood R. D., 2023b, Astrophysics Source Code Library, record ascl:2310.006

Ricker G. R. et al., 2015, J. Astron. Telesc. Instrum. Syst., 1, 014003

Robertson P., Mahadevan S., 2014, ApJ, 793, L24

Rosenthal L. J. et al., 2022, ApJS, 262, 1

Sekiguchi M., Fukugita M., 2000, AJ, 120, 1072

Skrutskie M. F. et al., 2006, AJ, 131, 1163

Sousa S. G., 2014, in Determination of Atmospheric Parameters of B. p. 297

Stalport M. et al., 2023, A&A, 678, A90

Stevens D. J., Gaudi B. S., 2013, PASP, 125, 933

Sugiura N., 1978, Communications in Statistics – Theory and Methods, 7, 13

Tayar J., Claytor Z. R., Huber D., van Saders J., 2022, ApJ, 927, 31

The LUVOIR Team, 2019, preprint (arXiv:1912.06219)

Torres G., Fischer D. A., Sozzetti A., Buchhave L. A., Winn J. N., Holman M. J., Carter J. A., 2012, ApJ, 757, 161

Tsantaki M., Sousa S. G., Adibekyan V. Z., Santos N. C., Mortier A., Israelian G., 2013, AAP, 555, A150

Unger N., Díaz R. F., Segránsan D., Delisle J. B., Hara N., 2020, Boletin de la Asociacion Argentina de Astronomia La Plata Argentina, 61B, 27

Van Eylen V., Agentoft C., Lundkvist M. S., Kjeldsen H., Owen J. E., Fulton B. J., Petigura E., Snellen I., 2018, MNRAS, 479, 4786

van Leeuwen F., 2007, A&A, 474, 653

Vitral E., Kremer K., Libralato M., Mamon G. A., Bellini A., 2022, MNRAS, 514, 806

Vogt S. S., Butler R. P., Rivera E. J., Haghighipour N., Henry G. W., Williamson M. H., 2010, ApJ, 723, 954

Weiss L. M. et al., 2024, ApJS, 270, 8

Wise A. W., Dodson-Robinson S. E., Bevenour K., Provini A., 2018, AJ, 156, 180

Wright E. L. et al., 2010, AJ, 140, 1868

Zechmeister M., Kürster M., 2009, A&A, 496, 577

Zhu W., Wu Y., 2018, AJ, 156, 92

SUPPORTING INFORMATION

Supplementary data are available at *MNRAS* online.

APPENDIX A: SOME EXTRA FIGURES

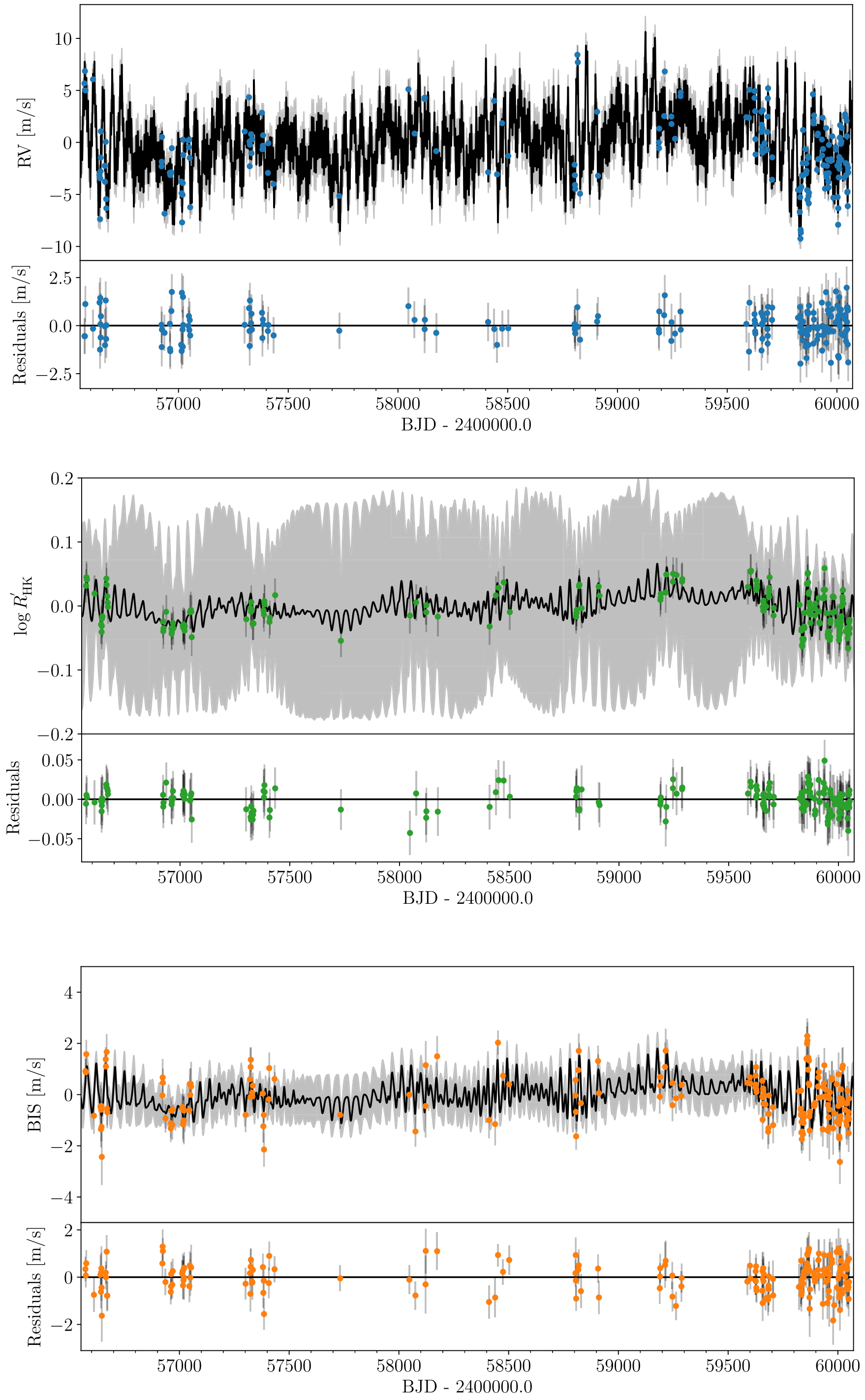

Figure A1. *Multi-dimensional GP analysis*: The figure illustrates the YVA RVs and the best-fitting model obtained through multidimensional GP regression. In the RV plot, the black line represents the modelled activity with three Keplerians, and the grey-shaded region denotes the $1-\sigma$ uncertainty on the model. The black lines in the log R'_{HK} and FWHM time series represent the modeled activity, revealing a recurring pattern. The residuals are displayed at the bottom of each plot.

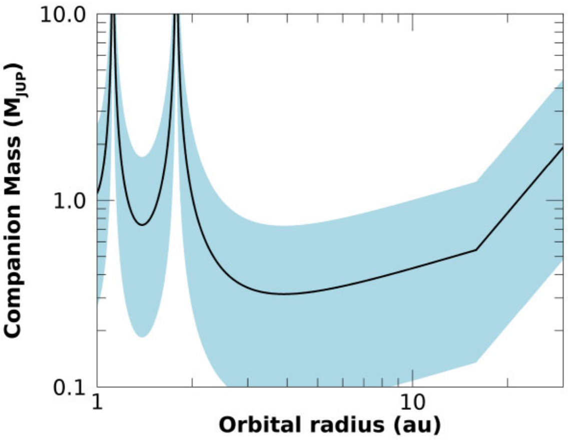

Figure A2. Sensitivity to companions of a given mass (in $M_{\rm Jup}$) as a function of the orbital semimajor axis (in au) orbiting HD 48948 based on the level of measured astrometric acceleration. The solid line identifies the combinations of mass and separation explaining the observed acceleration at the mean epoch of *Gaia* DR3 (Kervella et al. 2022), based on the analytical formulation of Kervella et al. (2019). The shaded light-blue region corresponds to the 1σ uncertainty domain.

Table A1. Likelihood comparison between the tested models in the injected Keplerian retrieval analysis described in Section 7.2. The runs are defined by the amplitude of the injected signal.

	0.38 m s^{-1}	1.06 m s^{-1}	1.75 m s^{-1}
	ln $\mathcal{L}$		
GP + Keplerian	− 282.99	− 280.66	− 279.84
GP only	−284.49	−289.27	−295.59
	AICc		
GP + Keplerian	587.21	582.55	580.91
GP only	579.30	588.87	601.51

[1] *Department of Astrophysics, University of Exeter, Stocker Rd, Exeter EX4 4QL, UK*
[2] *Department of Physics, University of Oxford, OX13RH Oxford, UK*
[3] *SUPA, School of Physics & Astronomy, University of St Andrews, North Haugh, St Andrews KY169SS, UK*
[4] *Dipartimento di Fisica e Astronomia 'Galileo Galilei' – Università degli Studi di Padova, Vicolo dell'Osservatorio 3, I-35122 Padova, Italy*
[5] *INAF - Osservatorio Astrofisico di Torino, via Osservatorio 20, I-10025 Pino Torinese, Italy*
[6] *Blue Skies Space, Italia SRL, via Vincenzo Monti 16, 20123, Milano, Italy*
[7] *Department of Astrophysics, University of Birmingham, Edgbaston, Birmingham B15 2TT, UK*
[8] *DTU Space, Technical University of Denmark, Elektrovej 328, DK-2800 Kgs. Lyngby, Denmark*
[9] *Observatoire de Genève, Université de Genève, Chemin Pegasi, 51, CH-1290 Versoix, Switzerland*
[10] *Astrophysics Group, Cavendish Laboratory, University of Cambridge, J.J. Thomson Avenue, Cambridge CB3 0HE, UK*
[11] *SUPA, Institute for Astronomy, The Royal Observatory, University of Edinburgh, Blackford Hill, Edinburgh EH9 3HJ, UK*
[12] *Centre for Exoplanet Science, University of Edinburgh, Edinburgh EH9 3FD, UK*
[13] *Kavli Institute for Astrophysics and Space Research, Massachusetts Institute of Technology, 77 Massachusetts Avenue, Cambridge, MA 02139, USA*
[14] *Centre for Exoplanet Science, University of St Andrews, North Haugh, St Andrews KY169SS, UK*
[15] *INAF – Osservatorio Astronomico di Palermo, Piazza del Parlamento, 1, I-90134, Palermo, Italy*
[16] *Fundación Galileo Galilei – INAF (Telescopio Nazionale Galileo), Rambla J. A. F. Perez 7, E-38712 Breña Baja (La Palma), Canary Islands, Spain*
[17] *Instituto de Astrofísica de Canarias, C/Vía Láctea s/n, E-38205 La Laguna (Tenerife), Canary Islands, Spain*
[18] *Departamento de Astrofísica, Universidad de La Laguna, Av. del Astrofísico Francisco Sánchez s/n, E-38205 La Laguna (Tenerife), Canary Islands, Spain*
[19] *Centre for Exoplanets and Habitability, University of Warwick, Gibbet Hill Road, Coventry CV4 7AL, UK*
[20] *Department of Physics, University of Warwick, Gibbet Hill Road, Coventry CV4 7AL, UK*
[21] *Center for Astrophysics, Harvard & Smithsonian, 60 Garden Street, Cambridge, MA 02138, USA*
[22] *Centre for Astrophysics, University Of Southern Queensland, West Str, Toowoomba, QLD 4350, Australia*
[23] *Space sciences, Technologies and Astrophysics Research (STAR) Institute, Université de Liège, Allée du Six-Août 19C, B-4000 Liège, Belgium*
[24] *Astrobiology Research Unit, Université de Liège, Allée du 6 Août 19C, B-4000 Liège, Belgium*
[25] *Astrophysics Research Centre, Queen's University Belfast, Belfast BT7 1NN, UK*

This paper has been typeset from a TEX/LATEX file prepared by the author.